



# Quantifying CH<sub>4</sub> emissions in hard coal mines from TROPOMI and IASI observations using the wind-assigned anomaly method

Qiansi Tu<sup>1,2</sup>, Matthias Schneider<sup>2</sup>, Frank Hase<sup>2</sup>, Farahnaz Khosrawi<sup>2</sup>, Benjamin Ertl<sup>2,3</sup>, Jaroslaw Necki<sup>4</sup>, Darko Dubravica<sup>2</sup>, Christopher J. Diekmann<sup>2,a</sup>, Thomas Blumenstock<sup>2</sup>, and Dianjun Fang<sup>1,5</sup>

<sup>1</sup>School of Mechanical Engineering, Tongji University, Shanghai, China

<sup>2</sup>Karlsruhe Institute of Technology (KIT), Institute of Meteorology and Climate Research (IMK-ASF), Karlsruhe, Germany

<sup>3</sup>Karlsruhe Institute of Technology, Steinbuch Centre for Computing (SCC), Karlsruhe, Germany

<sup>4</sup>AGH – University of Science and Technology, Krakow, Poland

<sup>5</sup>Qingdao Sino-German Institute of Intelligent Technologies, Qingdao, China

<sup>a</sup>now at: Software Solutions Department, Telespazio Germany GmbH, Darmstadt, Germany

**Correspondence:** Qiansi Tu (qiansi.tu@kit.edu) and Matthias Schneider (matthias.schneider@kit.edu)

Received: 15 January 2022 – Discussion started: 11 February 2022

Revised: 17 June 2022 – Accepted: 20 June 2022 – Published: 1 August 2022

**Abstract.** Intensive coal mining activities in the Upper Silesian Coal Basin (USCB) in southern Poland are resulting in large amounts of methane (CH<sub>4</sub>) emissions. Annual CH<sub>4</sub> emissions reached 448 kt according to the European Pollutant Release and Transfer Register (E-PRTR, 2017). As a CH<sub>4</sub> emission hotspot in Europe, it is of importance to investigate its emission sources and make accurate emission estimates.

In this study, we use satellite-based total column-averaged dry-air mole fraction of CH<sub>4</sub> (XCH<sub>4</sub>) from the Tropospheric Monitoring Instrument (TROPOMI) and tropospheric XCH<sub>4</sub> (TXCH<sub>4</sub>) from the Infrared Atmospheric Sounding Interferometer (IASI). In addition, the high-resolution model forecasts, XCH<sub>4</sub> and TXCH<sub>4</sub>, from the Copernicus Atmosphere Monitoring Service (CAMS) are used to estimate the CH<sub>4</sub> emission rate averaged over 3 years (November 2017–December 2020) in the USCB region (49.3–50.8° N and 18–20° E). The wind-assigned anomaly method is first validated using the CAMS forecast data (XCH<sub>4</sub> and TXCH<sub>4</sub>), showing a good agreement with the CAMS GLOBAL ANThropogenic emission (CAMS-GLOB-ANT) inventory. It indicates that the wind-assigned method works well. This wind-assigned method is further applied to the TROPOMI XCH<sub>4</sub> and TROPOMI + IASI TXCH<sub>4</sub> by using the Carbon dioxide and Methane (CoMet) inventory derived for the year 2018. The calculated averaged total CH<sub>4</sub> emissions over the USCB region is about 496 kt yr<sup>-1</sup> ( $5.9 \times 10^{26}$  molec. s<sup>-1</sup>) for TROPOMI XCH<sub>4</sub> and 437 kt yr<sup>-1</sup> ( $5.2 \times 10^{26}$  molec. s<sup>-1</sup>) for TROPOMI + IASI TXCH<sub>4</sub>. These values are very close to the ones given in the E-PRTR inventory (448 kt yr<sup>-1</sup>) and the ones in the CoMet inventory (555 kt yr<sup>-1</sup>), and are thus in agreement with these inventories. The similar estimates of XCH<sub>4</sub> and TXCH<sub>4</sub> also imply that for a strong source, the dynamically induced variations of the CH<sub>4</sub> mixing ratio in the upper troposphere and lower stratosphere region are of secondary importance. Uncertainties from different error sources (background removal and noise in the data, vertical wind shear, wind field segmentation, and angle of the emission cone) are approximately 14.8 % for TROPOMI XCH<sub>4</sub> and 11.4 % for TROPOMI + IASI TXCH<sub>4</sub>. These results suggest that our wind-assigned method is quite robust and might also serve as a simple method to estimate CH<sub>4</sub> or CO<sub>2</sub> emissions for other regions.

## 1 Introduction

Atmospheric methane (CH<sub>4</sub>) is the second most important anthropogenic greenhouse gas (GHG) with a larger global warming potential than carbon dioxide (CO<sub>2</sub>) (IPCC, 2014). The globally averaged amount of atmospheric CH<sub>4</sub> has increased by 260 % to  $1877 \pm 2$  ppb from the preindustrial era until 2019 (World Meteorological Organization, 2020). Sources of CH<sub>4</sub> induced by anthropogenic activities include fossil fuel production and use (e.g., coal mining, gas/oil extraction), waste disposal, and agriculture, which in total accounts for about 60 % of the total CH<sub>4</sub> emissions (Saunois et al., 2020). Although most sources and sinks of CH<sub>4</sub> have been characterized, their spatial–temporal variations and relative contributions to the atmospheric CH<sub>4</sub> level are still highly uncertain (Kirschke et al., 2013; Saunois et al., 2020).

Approximately 33 % of the CH<sub>4</sub> emissions from coal mining ( $42\,000 \text{ kt yr}^{-1}$ ) are estimated to come from the total fossil-fuel-related emissions during 2008–2017 (Saunois et al., 2020). The CH<sub>4</sub> is released primarily to the atmosphere via ventilation shafts located at the surface during the production and processing of the coal (Saunois et al., 2020; Andersen et al., 2021). The largest contribution of CH<sub>4</sub> emissions related with the coal mining activities in Europe is from southern Poland – the Upper Silesian Coal Basin (USCB) (Luther et al., 2019; Krautwurst et al., 2021). The USCB is in the Silesian Upland, which is a plateau between 200 and 300 m above sea level (m.a.s.l.) with a predominant southwest wind. The USCB within Poland covers an area of over 5800 km<sup>2</sup>, and to its south is the Tatra Mountains ridge with elevations larger than 2000 m.a.s.l. The European Pollutant Release and Transfer Register (E-PRTR, 2017; <https://prtr.eea.europa.eu/>, last access: 25 October 2021) reports that the total CH<sub>4</sub> emissions from the USCB region amount to  $448 \text{ kt yr}^{-1}$ . Most of these emissions are from mining activities and heavy industry (Kostinek et al., 2021), which makes this region a hot spot for CH<sub>4</sub> emissions in Europe.

To investigate the CH<sub>4</sub> emissions from this hot spot, the Carbon Dioxide and Methane (CoMet) campaign was performed, covering roughly 3 weeks from May to June 2018. A variety of state-of-the-art instruments, including in situ and remote-sensing instruments on the ground and aboard five research aircraft, were deployed in order to provide independent observations of GHG emissions on local to regional scale and provide data for satellite validation (more details can be found in Luther et al., 2019; Fiehn et al., 2020; Gałkowski et al., 2021b; Kostinek et al., 2021; Krautwurst et al., 2021; Wolff et al., 2021). For example, Gałkowski et al. (2021b) present results of in situ GHG measurements obtained over nine research flights of the German research aircraft, HALO (High Altitude and Long Range Research Aircraft), acting as the airborne flagship of the CoMet campaign, together with simultaneous flask measurements for the iso-

topic composition of CH<sub>4</sub>. A new lidar, CHARM-F (CO<sub>2</sub> and CH<sub>4</sub> Atmospheric Remote Monitoring Flugzeug), was also on board HALO and its measurements were investigated to determine CO<sub>2</sub> emission rates from the power plant (Wolff et al., 2021). Many studies present similar CH<sub>4</sub> emission estimates for the region based on different instruments and methods. Luther et al. (2019) estimated CH<sub>4</sub> emissions ranging from  $6 \pm 1 \text{ kt yr}^{-1}$  for a single shaft up to  $109 \pm 33 \text{ kt yr}^{-1}$  for a subregion of USCB covering several shafts, by using several portable Fourier transform infrared (FTIR) spectrometers (Bruker EM27/SUN). Active AirCore system aboard an unmanned aerial vehicle (UAV) was used to measure CH<sub>4</sub> downwind of a single ventilation shaft, and emission rates ranging from 0.5 to  $14.5 \text{ kt yr}^{-1}$  based on a mass balance approach and ranging from 1.1 to  $9.0 \text{ kt yr}^{-1}$  based on an inverse Gaussian method were estimated (Andersen et al., 2021). Fiehn et al. (2020) analyzed aircraft- and ground-based in situ observations and reported an emission estimate of  $436 \pm 115 \text{ kt yr}^{-1}$  and  $477 \pm 101 \text{ kt yr}^{-1}$  from two selected flights. An advanced model approach was introduced by Kostinek et al. (2021) to investigate two research flights in the morning and afternoon, resulting in estimated CH<sub>4</sub> emissions of  $451 \pm 77 \text{ kt yr}^{-1}$  and  $423 \pm 79 \text{ kt yr}^{-1}$ , respectively. Another emission estimate based on the observations from the nadir-looking passive remote sensing Methane Airborne MAPper (MAMAP) instrument accounted for 8.8 to  $78.8 \text{ kt yr}^{-1}$  for sub-clusters of ventilation shafts (Krautwurst et al., 2021). A recent study (Luther et al., 2022) displays a larger emission rate of  $414\text{--}790 \text{ kt yr}^{-1}$  based on a network of four portable Fourier-transform spectrometer (FTS) instruments (EM27/SUN) during the CoMet campaign.

Launched in October 2017, the Tropospheric Monitoring Instrument (TROPOMI) on board the Sentinel-5 Precursor satellite provides an unprecedented high spatial resolution ( $5.5 \times 7 \text{ km}^2$ ) of the CH<sub>4</sub> total column-averaged dry-air mole fraction (XCH<sub>4</sub>) (Veefkind et al., 2012; Lorente et al., 2021a). An a posteriori method has been developed by Schneider et al. (2022a) to obtain tropospheric XCH<sub>4</sub> (TXCH<sub>4</sub>) by combining observations from TROPOMI and the Infrared Atmospheric Sounding Interferometer (IASI). This synergetic product is not influenced by the changing tropopause height, and it offers improved sensitivity to the tropospheric variations than the total column XCH<sub>4</sub> data from either sensor. The improved real-time forecast data with high resolution ( $0.1^\circ \times 0.1^\circ \sim 9 \text{ km} \times 9 \text{ km}$ ) are produced by the Copernicus Atmosphere Monitoring Service (CAMS) (Agustí-Panareda et al., 2019; Barré et al., 2021). All data sets provide a large spatial coverage and long-term XCH<sub>4</sub>/TXCH<sub>4</sub> observations, which help to better estimate CH<sub>4</sub> emissions in the USCB region.

In Sect. 2 we present the data sets and methodology used in this study to derive estimated CH<sub>4</sub> emissions. The results and discussions are presented in Sect. 3. We present a

novel wind-assigned method introduced by Tu et al. (2022), which is firstly verified by the CAMS model forecasts and then applied to the TROPOMI XCH<sub>4</sub> and TROPOMI + IASI TXCH<sub>4</sub> data to estimate the CH<sub>4</sub> emissions in the USCB region for the time period from November 2017 to December 2020, together with an uncertainty analysis. Finally, the summary and conclusions are given in Sect. 4.

## 2 Data sets and method

There are over 50 active ventilation shafts in the USCB region (49.3–50.8° N and 18–20° E), Poland, whose emission rates range between 0.17 and 41.02 kt yr<sup>-1</sup> (Gałkowski et al., 2021a) (Fig. 4b). Most of them are located near Katowice and further west and southwest of Katowice.

### 2.1 CAMS CH<sub>4</sub> forecast and emission inventories

The Integrated Forecasting System (IFS, <https://www.ecmwf.int/en/publications/ifs-documentation>, last access: 27 October 2021) from the European Centre for Medium-Range Weather Forecasts (ECMWF) is used in the CAMS atmospheric composition analysis and forecasts system to simulate 5 d CO<sub>2</sub> and CH<sub>4</sub> forecasts (Agustí-Panareda et al., 2019, Barré et al., 2021), as well as other chemical species and aerosols (Flemming et al., 2015; Morcrette et al., 2009). This model is also used in the operational Numerical weather prediction (NWP) system, but with additional modules (Agustí-Panareda et al., 2019). The forecast data used in this study are the same suit as the data used in Barré et al. (2021), where the Cycle 45r1 IFS model cycle was implemented. The CAMS GHGs operational data set includes analysis and forecast data at medium and high resolution, with 137 model levels from the surface to 0.01 hPa (Barré et al., 2021). In this study we will focus on using the high-resolution CH<sub>4</sub> forecasts, which have a spatial resolution of 0.1° × 0.1° and a temporal resolution of 3 h, starting from 00:00 UTC. Here we use the daily averaged CAMS forecasts during 09:00–18:00 UTC at each resolution grid point. The corresponding standard deviation (SD) is considered as the noise/error.

The anthropogenic CH<sub>4</sub> emissions used in the global CAMS forecasts are from the CAMS-GLOB-ANT inventory (Granier et al., 2019; <https://permalink.aeris-data.fr/CAMS-GLOB-ANT>, last access: 27 October 2021). The CAMS-GLOB-ANT inventory is based on the emissions provided by the Emissions Database for Global Atmospheric Research (EDGAR) v4.3.2 inventory for the 2000–2012 time period (Crippa et al., 2018), and linearly extrapolated to 2020 using the trends from the Community Emissions Data System (CEDA) global inventory for the 2011–2014 time period (Hoesly et al., 2018). The latest version (CAMS-GLOB-ANT v4.2) was released in March 2020, using the same setup as v4.1, except for adding the emissions in 2020. The anthropogenic sources in the standard v4.2 are divided into 12 sectors and the agricultural sections are split into three

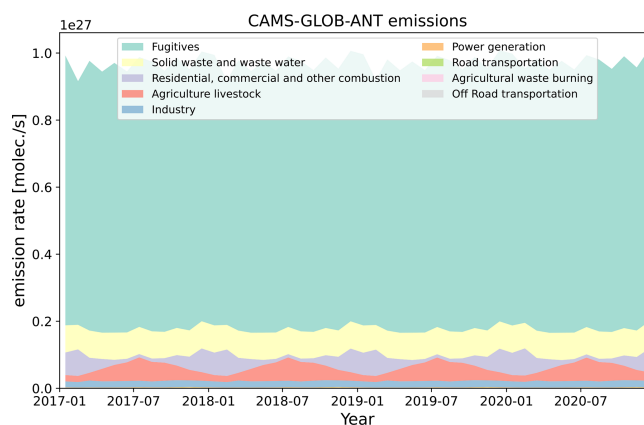


**Figure 1.** Stacked area plot for different sectors of the monthly averaged CAMS global anthropogenic emissions ( $> 1 \times 10^{20}$  molec. s<sup>-1</sup>) in the USCB region for 2017–2020 (<https://permalink.aeris-data.fr/CAMS-GLOB-ANT>, last access: 22 December 2021, Granier et al., 2019).

sectors, including livestock, soils and waste burning (<https://eccad3.sedoo.fr/>, last access: 27 October 2021). The inventory is provided as a monthly mean with the same spatial resolution (0.1° × 0.1°) as the CAMS forecast data (Granier et al., 2019).

The monthly averages of CAMS-GLOB-ANT for different sectors in the study area of USCB are presented in Fig. 1. The emissions from the sectors “agricultural soils” and “solvents” are zeros. The CH<sub>4</sub> emitted from ships has 19 orders of magnitude, which are much lower than the other sectors. Thus, these three sectors are not shown here. The sources from agricultural livestock ( $1.7 \times 10^{25} \pm 4.0 \times 10^{25}$  molec. s<sup>-1</sup>) amount to only 4 % of the total emissions in this region. The dominant CH<sub>4</sub> sources in this region are fugitive sources from energy production and distribution (e.g., fuel use). With a mean value of  $7.9 \times 10^{26}$  molec. s<sup>-1</sup> and SD of  $2.2 \times 10^{25}$  molec. s<sup>-1</sup>, they account for 82 % of the anthropogenic CH<sub>4</sub> emissions in the CAMS-GLOB-ANT inventory ( $9.7 \times 10^{26}$  molec. s<sup>-1</sup> in total). This becomes particularly visible in the spatially overlapping distribution within USCB (see Fig. 2). The seasonal emission variations of the fugitive sector are minor and can be ignored. Therefore, we apply the 3-year mean of total emissions at grids with significant emissions without considering seasonal variations in the simple cone plume model (see Sect. 2.3). The total emissions amount to  $9.7 \times 10^{26}$  molec. s<sup>-1</sup> over this study area.

### 2.2 TROPOMI and IASI data sets

The TROPOMI instrument is a nadir-viewing, imaging spectrometer, which uses passive remote-sensing techniques to perform measurements of the solar radiation reflected by and radiated from the Earth in the ultraviolet (UV), the visible (VIS), the near-infrared (NIR), and the short-wave infrared spectral (SWIR) bands (Veefkind et al., 2012). The instru-

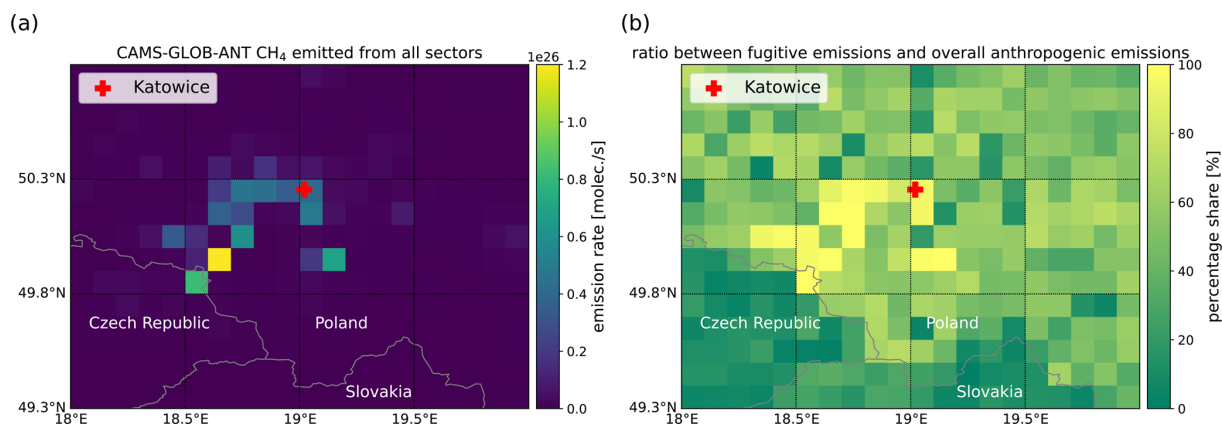


**Figure 2.** Spatial distribution of (a) the CAMS global anthropogenic emissions (CAMS-GLOB-ANT) from all sectors and (b) percentage share of the fugitive emissions compared to the overall anthropogenic emissions over the USCBA region on a  $0.1^\circ \times 0.1^\circ$  latitude/longitude grid. The fugitives are the dominant CH<sub>4</sub> sources.

ment crosses the Equator at about 13:30 LST at each orbit with a repeat cycle of 17 d. It observes a full swath (2600 km) per second with an orbital duration of 100 min. The algorithm for CH<sub>4</sub> column retrieval is called the RemoTeC algorithm and it has been extensively used to derive CO<sub>2</sub> and CH<sub>4</sub> retrievals from the Greenhouse Gases Observing Satellite (GOSAT) and Orbiting Carbon Observatory-2 (OCO-2; Boesch et al., 2011; Butz et al., 2009, 2011; Hasekamp and Butz, 2008; Schepers et al., 2012). An updated retrieval algorithm has been implemented by Lorente et al. (2021a) to obtain a data suit with less scatter and a higher-resolution surface altitude database. This updated TROPOMI XCH<sub>4</sub> data set has been validated with the Total Carbon Column Observing Network (TCCON) ( $-3.4 \pm 5.6$  ppb) and GOSAT ( $-10.3 \pm 16.8$  ppb), showing very good agreements. In this study, the TROPOMI XCH<sub>4</sub> during November 2017 and December 2020 within the study area over the USCBA region is investigated. The data provided by Lorente et al. (2021a) include an additional quality filter parameter (quality value,  $q_a$ ). The TROPOMI XCH<sub>4</sub> with  $q_a = 1.0$  represents the data under clear-sky and low-cloud atmospheric conditions and the problematic data points are removed as well. This quality filter has been applied in this study and about 16 000 data are derived over the 3-year time period considered in this study.

The IASI instrument is a nadir viewing FTS that measures the infrared part of the electromagnetic spectrum. The IASI measurements are performed with a horizontal resolution of 12 km and a full swath width of about 2200 km on the ground. It is the key payload element of the polar-orbiting METOP-A -B and -C satellites. These satellites overpass the Equator at 09:30 LT and 21:30 LT, with about 14 orbits per day. It provides unprecedented accurate vertical information of atmospheric temperature and humidity, which helps to improve NWP (Collard, 2007; Coopmann et al., 2020). The thermal infrared nadir spectra of IASI have been successfully used in retrieving different atmospheric trace gas pro-

files, and these retrievals are especially sensitive between the middle troposphere and the stratosphere (García et al., 2018; Diekmann et al., 2021; Schneider et al., 2022a, 2022b). By combining the IASI CH<sub>4</sub> profiles and the TROPOMI CH<sub>4</sub> total column, which has a higher sensitivity near ground, we are able to detect the TXCH<sub>4</sub> independently from CH<sub>4</sub> at higher altitudes. The combined product cannot be obtained by either the TROPOMI or IASI product independently. The combined product shows a weak positive bias of about 1 % with respect to the reference data (Schneider et al., 2022a). We refer to this product in the following as the TROPOMI + IASI TXCH<sub>4</sub> and it comprises about 12 000 data points for the time period considered in this study.

### 2.3 Simple cone plume model and wind-assigned anomaly method

The averaged distribution of emitted CH<sub>4</sub> over a long-term period can be modeled simply as an evenly distributed cone-shape dispersion based on the wind and source strength. Since CH<sub>4</sub> is a long-lived gas, its decay is negligible for short periods and not considered in the model. This model is referred to as the simple cone plume model (see Fig. A1). This model is easy to apply, and the estimated emission strengths are reasonable compared to the ones from other studies (Tu et al., 2022).

Based on the simple cone plume model, the enhanced CH<sub>4</sub> column ( $\Delta\text{CH}_4$ ) at the downwind side of the location ( $x_i, y_i$ ) is computed as

$$\Delta\text{CH}_4(x_i, y_i) = \frac{\varepsilon}{v \cdot d(x_i, y_i) \cdot \alpha}, \quad (1)$$

where the emission strength  $\varepsilon$  is the a priori knowledge from the CAMS-GLOB-ANT data set or from the coal mine ventilation shafts in this study (see Sect. 3.2). Their emission rates are assumed to be constant with time from 2017 to

2020. The angle of the emission cone is  $\alpha$  and has an empirical value of  $60^\circ$ , which has been derived from TROPOMI NO<sub>2</sub> measurements (Tu et al., 2022). The wind speed from ERA5,  $v$ , is the fifth generation ECMWF reanalysis product using 4D-Var data assimilation and model forecasts in Cycle 41R2 of the ECMWF IFS model (Copernicus Climate Change Service, C3S, 2017; Hersbach et al., 2020). The ERA5 provides hourly estimates on 137 pressure levels in the vertical covering the atmosphere from the surface up to 0.01 hPa, with a spatial resolution of  $0.25^\circ \times 0.25^\circ$  (Hersbach et al., 2020). The distance between the downwind location and the CH<sub>4</sub> emission source is denoted as  $d$ . Each individual source, either from the CAMS-GLOB-ANT inventory or from the knowledge of the ventilation shafts, is considered as an individual point source. The daily plume from each point source (location at  $(i, j)$ ) is averaged over daytime (08:00–18:00 UTC):

$$\overline{\text{XCH}_4}_{(i,j)} = \frac{1}{11} \sum_{t=1}^{11} \text{XCH}_4_{(i,j),t}. \quad (2)$$

These daily plumes are super-positioned over all point sources to obtain a daily plume ( $\overline{\text{XCH}_4}_{\text{daily}}$ ):

$$\overline{\text{XCH}_4}_{\text{daily}} = \sum_{s=1}^{N_s} \overline{\text{XCH}_4}_{(i,j),s}, \quad (3)$$

where  $N_s$  represents the number of the sources.

The wind distributions at different height levels (10,  $\sim$  330,  $\sim$  500 m) over the USCB region are presented in Fig. 3. The wind speed increases with increasing altitude (see Table 1). The ERA5 wind is divided into two opposite wind regimes based on directions (e.g.,  $135\text{--}315^\circ$  for SW and the rest for NE). For each wind regime, an averaged plume is computed:

$$\overline{\text{XCH}_4}_{\text{SW/NE}} = \frac{1}{N_d} \sum_{d=1}^{N_d} \overline{\text{XCH}_4}_{\text{daily},d}, \quad (4)$$

where  $N_d$  is the number of days with SW wind or NE wind.

The difference of the two plumes is therefore the wind-assigned anomaly:

$$\text{wind - assigned anomaly} = \overline{\text{XCH}_4}_{\text{NE}} - \overline{\text{XCH}_4}_{\text{SW}}. \quad (5)$$

The estimated emission strengths can be calculated by fitting the modeled anomalies to the known anomalies from e.g., CAMS XCH<sub>4</sub>/TXCH<sub>4</sub>, TROPOMI, and TROPOMI + IASI observations. Note that CH<sub>4</sub> has a lifetime of around 12 years, which results in a high background concentration compared to the newly emitted CH<sub>4</sub>. Thus, the contributions from the background should be removed for correctly estimating emissions (Liu et al., 2021). The background is considered to consist of a constant value, a linear increase with time, a seasonal cycle, a daily anomaly, and a horizontal anomaly. For more details, see the Appendix in Tu et al. (2022). The uncertainties ( $\pm$  values) in the emission estimate are determined by considering the deficits of the

background model due to the imperfect elimination of the background and the noise in the data set.

This method was firstly used to estimate the CH<sub>4</sub> emissions from landfills in Madrid, Spain based on nearly 3-year spaceborne XCH<sub>4</sub> data, and different opening angles were investigated to obtain an empirical value ( $60^\circ$ ) (Tu et al., 2022). The CH<sub>4</sub> emission strengths derived from satellite products have the same orders of magnitude as the ones from single-day observations by ground-based instruments, showing that this method works properly.

### 3 Results and discussion

#### 3.1 Estimated emissions derived from CAMS forecasts (evaluation of the method)

The CAMS forecast XCH<sub>4</sub> data from November 2017 to December 2020 within the study area are illustrated in Fig. 4 left. The areas with high XCH<sub>4</sub> amounts fit well with the CAMS anthropogenic CH<sub>4</sub> emissions (square symbols). Similar to the CoMet inventory, high sources in the CAMS-GLOB-ANT inventory are centered in this region, but there are other weaker sources outside. The total emission rate of the CoMet inventory is  $555 \text{ kt yr}^{-1}$  ( $6.6 \times 10^{26} \text{ molec. s}^{-1}$ ), which is slightly less than the CAMS-GLOB-ANT emissions ( $815 \text{ kt yr}^{-1}$ ). This is probably because the CAMS-GLOB-ANT includes more CH<sub>4</sub> emission sources, e.g., wastes and combustion (residential and commercial), which account for about 20 %.

Based on the CAMS emissions, the wind-assigned method is applied to CAMS XCH<sub>4</sub>. The XCH<sub>4</sub> enhancement (raw-background) and the wind-assigned anomalies are presented in Fig. 5a and b, respectively. The example plumes of the enhancements for wind coming from NE and SW are presented in Fig. A3. Note that the CAMS XCH<sub>4</sub> is coincided with TROPOMI XCH<sub>4</sub> for better comparison. Some data are thus missing here mostly due to the quality filter of TROPOMI observations. After removing the XCH<sub>4</sub> background, the XCH<sub>4</sub> anomalies represent the CAMS sources well. The highest CH<sub>4</sub> sources from the CAMS-GLOB-ANT inventory are also obviously visible in the 2D anomalies. In addition, the spatial distributions of the three XCH<sub>4</sub> data products show different patterns (Fig. 4), whereas the anomalies' (after removing background) patterns are similar (Figs. 5a and d, 7a and d). This indicates that the background removal is of importance for XCH<sub>4</sub> and our method works well.

The wind-assigned anomalies for CAMS and the simple cone plume model show a very good agreement with a slope of 1.11 and a  $R^2$  of 0.85 (Fig. 5c). Our results are derived from the CAMS emission information, and they are in good agreement with the CAMS model data. The estimated emission rate is about  $815 \pm 1 \text{ kt yr}^{-1}$  ( $9.7 \times 10^{26} \pm 2.0 \times 10^{25} \text{ molec. s}^{-1}$ ) when using the ERA5 wind at 975 hPa ( $\sim$  330 m), and this value is quite close to CAMS-GLOB-ANT (estimated emission rate at other levels are presented

**Table 1.** Number of days and the averaged wind speed ( $\pm$  standard deviation) per specific wind regime during daytime (08:00–18:00 UTC) at different vertical levels from November 2017 to December 2020 over the USCB region. The days for the 3-year average coincide with the TROPOMI overpass days.

	NE/ $> 315^\circ$ or $< 135^\circ$		SW/ $135\text{--}315^\circ$	
	Number of days in total (%)	Averaged wind speed $\pm$ standard deviation ( $\text{m s}^{-1}$ )	Number of days in total (%)	Averaged wind speed $\pm$ standard deviation ( $\text{m s}^{-1}$ )
10 m	39.1	$3.2 \pm 1.5$	56.9	$3.4 \pm 1.6$
$\sim 330$ m (975 hPa)	38.7	$4.1 \pm 2.2$	56.9	$4.3 \pm 2.3$
$\sim 500$ m (950 hPa)	38.7	$5.0 \pm 2.7$	57.3	$5.9 \pm 3.5$

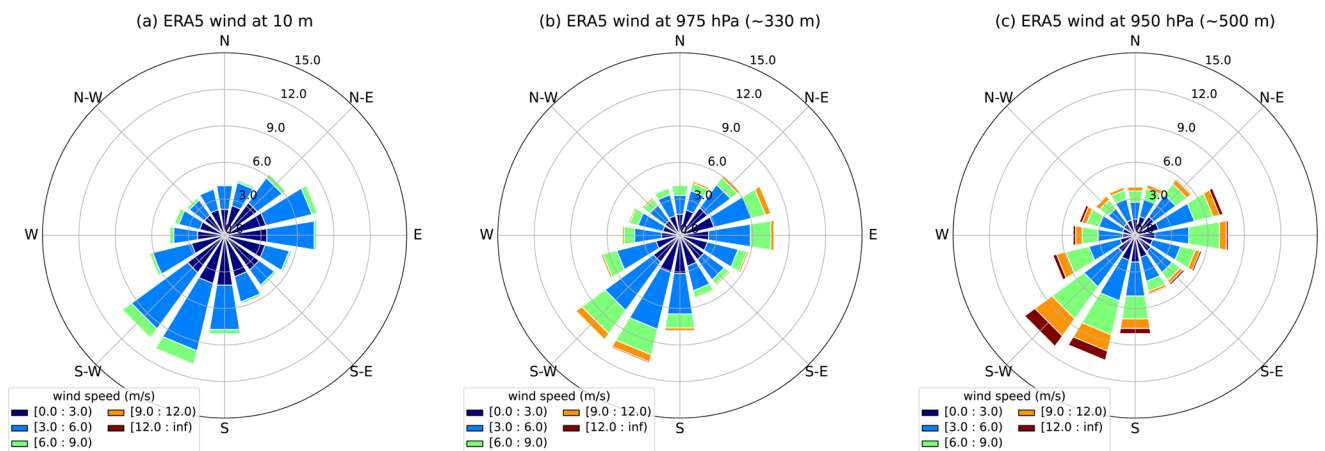


**Figure 3.** Wind rose plots for daytime (08:00–18:00 UTC) from November 2017 to December 2020 for the ERA5 model wind at different vertical levels (10,  $\sim 330$  and  $\sim 500$  m). The days for the 3-year average coincide with the TROPOMI overpass days.

in Sect. 3.2, see Fig. 8 as well). Therefore, we use ERA5 wind at this level in the following study. Note that the points whose distances to the nearest dominant sources are less than 10 km, are removed here, because they are very close to the significant sources and small changes in wind (either speed or direction) can result in high uncertainties.

The XCH<sub>4</sub> is affected by local surface emissions and a varying stratospheric contribution due to changes in the tropopause altitude (Liu et al., 2021; Schneider et al., 2022a). This stratospheric contribution has to be taken into account, in order to use XCH<sub>4</sub> for a reliable investigation of local surface CH<sub>4</sub> sources and sinks (Pandey et al., 2016). Our background removal method effectively accounts for the stratospheric contribution. To show this, we apply the approach to CAMS forecasts of XCH<sub>4</sub> (which has a significant stratospheric contribution) and TXCH<sub>4</sub> (calculated from the CAMS forecast as CH<sub>4</sub> averaged from surface to 6 km, which should have a very limited stratospheric contribution). The results are presented in Fig. 5d–f. The CAMS TXCH<sub>4</sub> anomalies have similar distribution as CAMS XCH<sub>4</sub> anomalies, suggesting that our background removal approach reliably removes the stratospheric contribution. The wind-assigned plume and the correlation between CAMS and the wind-assigned model results are very similar between XCH<sub>4</sub>

and TXCH<sub>4</sub>. The estimated CH<sub>4</sub> emission strength derived from CAMS TXCH<sub>4</sub> is  $798 \pm 15 \text{ kt yr}^{-1}$  ( $9.5 \times 10^{26} \pm 1.8 \times 10^{25} \text{ molec. s}^{-1}$ ).

### 3.2 Estimated emissions derived from satellite observations

The high-resolution TROPOMI XCH<sub>4</sub> provides the ability to detect and quantify the CH<sub>4</sub> emissions (e.g., oil and gas sector, coal mining) on fine and large scales (Pandey et al., 2019; Varon et al., 2019; De Gouw et al., 2020; Schneising et al., 2020). Figure 6 illustrates the enhanced XCH<sub>4</sub> (raw XCH<sub>4</sub>-background in the upwind) distribution over the USCB region on an example day (6 June 2018), in which the wind mostly came from northeast. As expected, obvious XCH<sub>4</sub> enhancements were observed by TROPOMI along the downwind direction (southwest of Katowice where most ventilation shafts are located), as well as simulated by the CAMS forecast. The downwind-enhanced XCH<sub>4</sub>, modeled by our simple cone plume model and based on the CAMS-GLOBANT inventory, also shows a similar shape of plume. This enhancement was also observed by portable FTIR instruments (COCCON) employed during the CoMet campaign (Fig. 4 in Luther et al., 2019). The observations support the state-

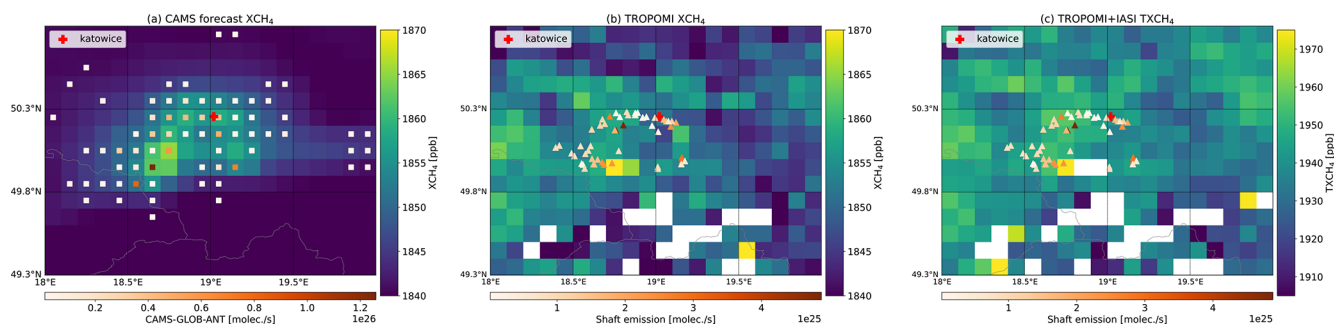


**Figure 4.** Averaged (a) CAMS forecast XCH<sub>4</sub>, (b) TROPOMI XCH<sub>4</sub>, and (c) TROPOMI + IASI TXCH<sub>4</sub> in the USCB region on a  $0.1^\circ \times 0.1^\circ$  latitude/longitude grid during November 2017–December 2020. The square and triangle symbols represent the locations of CAMS-GLOB-ANT sources (for better viewing, only the emission strengths larger than  $1 \times 10^{24}$  molec. s<sup>-1</sup> are shown here) and the active coal mine shafts from the CoMet inventory (Gałkowski et al., 2021a), respectively. Different colors denote the amount of emission rates. The white grids represent no data from TROPOMI or the number of the points in the grid less than 5. A zoomed version of panel (b) is shown in the appendix (Fig. A2). Note that a different color bar has been used in panel (c).

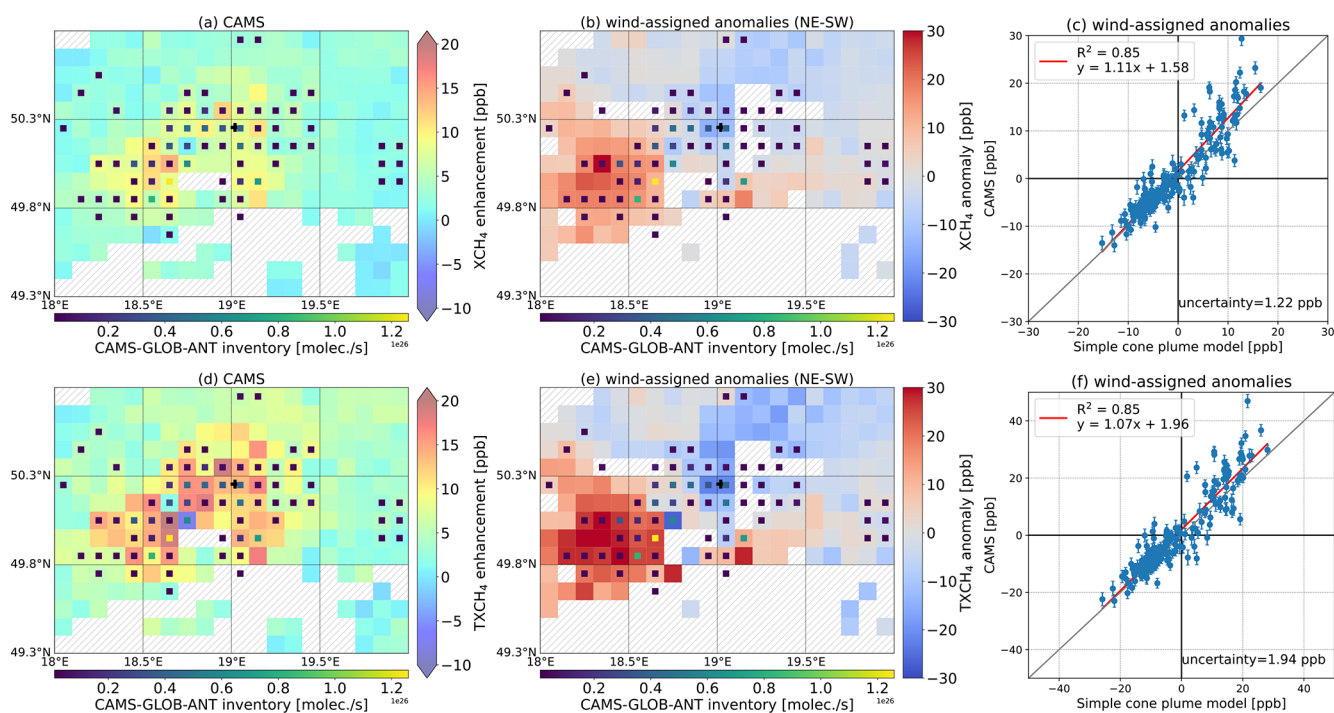


**Figure 5.** CAMS XCH<sub>4</sub> enhancement (XCH<sub>4</sub>-background) (a), the wind-assigned anomalies (NE–SW) (b), and correlation plot of the wind-assigned anomalies (c) between CAMS and the simple cone plume model with using the CAMS-GLOB-ANT inventory ( $9.7 \times 10^{26}$  molec. s<sup>-1</sup> in total) and ERA5 wind at 330 m during November 2017–December 2020 over the USCB region. The same as for the upper panel are shown in (d–f) but for CAMS TXCH<sub>4</sub>. The square symbols represent the locations of the CAMS-GLOB-ANT ( $> 1 \times 10^{24}$  molec. s<sup>-1</sup>) inventory and different colors denote the amount of emission rates. The hatched areas in (a)–(b) and (d)–(e) represent no data in these grids. The uncertainties in (c) and (f) represent the mean error bars, i.e., error propagation of the background uncertainty and the CAMS standard deviation.

ment that TROPOMI is able to detect the CH<sub>4</sub> emission signals. In addition, the spatial pattern of the downwind plume is similar to that of the cone-shaped plume, which implies our cone-shape assumption is reasonable.

The 3-year averaged TROPOMI XCH<sub>4</sub> observations presented in Fig. 4b show scattered high XCH<sub>4</sub> amounts,

whereas CAMS XCH<sub>4</sub> is more concentrated on the center of the study area, and those agree well with its anthropogenic emission sources (CAMS-GLOB-ANT inventory). This might be because TROPOMI detects other real CH<sub>4</sub> sources that are not included in the CAMS forecast model data.

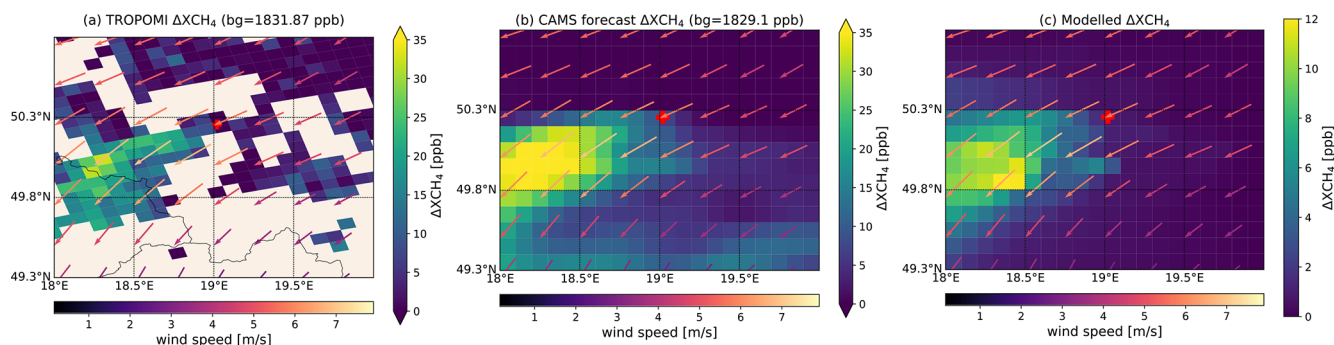


**Figure 6.**  $\Delta\text{XCH}_4$  together with the ERA5 wind at 12:00 UTC from (a) TROPOMI observations at 11:34 UTC, (b) CAMS forecast at 12:00 UTC, and (c) from the simple cone plume model (averaged over the daytime) based on the CAMS-GLOB-ANT inventory over the USC region on an example day (6 June 2018). The “bg” in the title of (a) and (b) represents the average background, derived from the mean  $\text{XCH}_4$  in the upwind region ( $50.3\text{--}50.8^\circ\text{N}$ ,  $19.5\text{--}20.0^\circ\text{E}$ ). Note that a different color bar has been used in panel (c) for improved recognizability.

For better comparison with other studies discussing the coal mine emissions in the USC region, we apply the CoMet inventory as the a priori known sources in the wind-assigned method to estimate the  $\text{CH}_4$  emissions. The results are illustrated in Fig. 7. The TROPOMI  $\text{XCH}_4$  and TROPOMI + IASI  $\text{TXCH}_4$  anomalies show high concentrations around the areas where the ventilation shafts are located and the region in the northeast of Katowice. Although the anomalies of the satellite observations are lower than the CAMS results (Fig. 5a), their spatial distributions are similar. Positive and negative plumes can be clearly seen in Fig. 7b and e. The correlation of the wind-assigned anomalies between the TROPOMI and simple cone plume model has a very good agreement with an  $R^2$  value of 0.76. Similar results are also derived from TROPOMI + IASI  $\text{TXCH}_4$  with a  $R^2$  value of 0.62. Compared to CAMS data, higher scatter is expected, because satellite observations suffer from observational errors and might contain more  $\text{CH}_4$  sources (e.g., landfills, gas distribution network). Although none of these sources have the same orders of magnitude of coal mining emission, they might still bring some errors.

The estimated  $\text{CH}_4$  emission strengths are  $496 \pm 17 \text{ kt yr}^{-1}$  ( $5.9 \times 10^{26} \pm 2.1 \times 10^{25} \text{ molec. s}^{-1}$ ) for  $\text{XCH}_4$  and  $437 \pm 27 \text{ kt yr}^{-1}$  ( $5.2 \times 10^{26} \pm 3.2 \times 10^{25} \text{ molec. s}^{-1}$ ) for  $\text{TXCH}_4$ , and both are close to the E-PRTR inventory ( $448 \text{ kt yr}^{-1}$ ). The TROPOMI + IASI result has a higher uncertainty than the TROPOMI result, because (1) the vertical distribution of  $\text{CH}_4$  is in general much more difficult to measure than the total column of  $\text{CH}_4$  and (2) the vertical distribution is derived by considering two independent measurements, each with its own noise error. This might change for a larger number of data points (e.g., by using data from more years or by applying the method to IASI and TROPOMI successors on the upcoming METOP-SG satellite, which offers much more collocated observations).

However, in our study, using  $\text{TXCH}_4$  data in addition to  $\text{XCH}_4$  data nicely documents the robustness of the method.

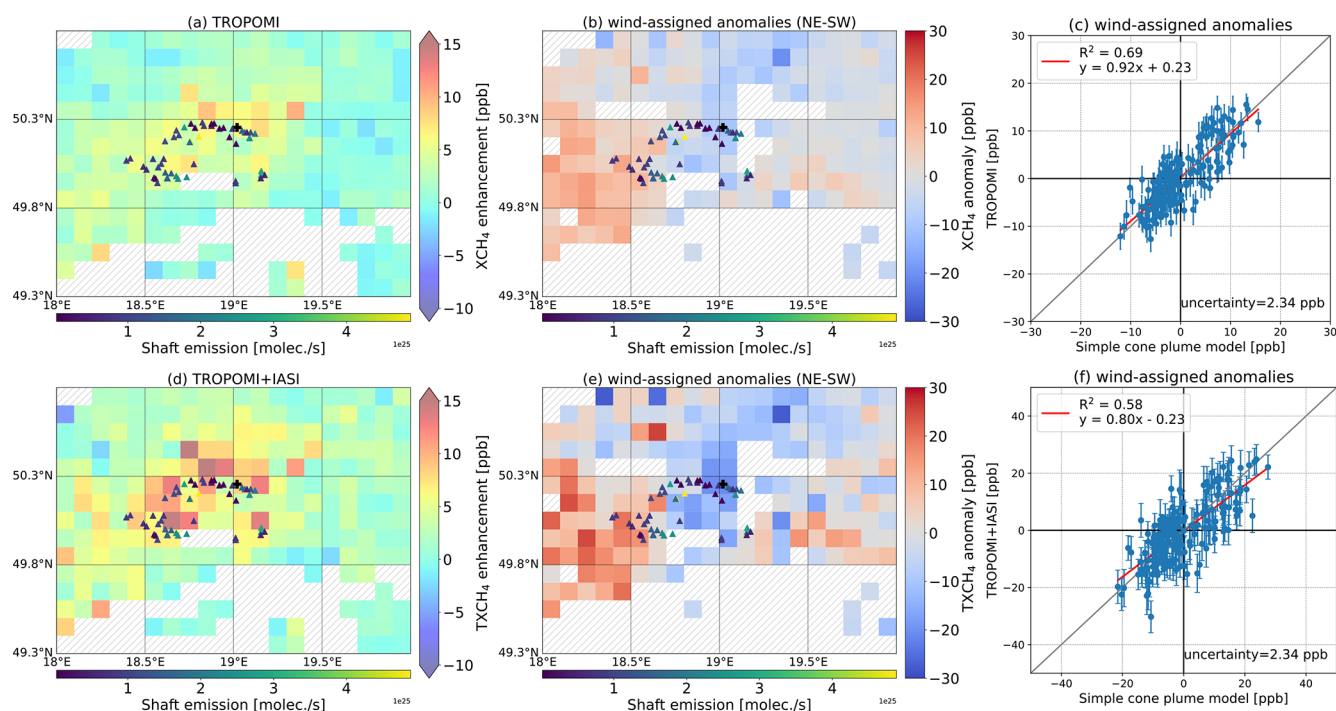
Important for a correct estimation of the emission is the correct removal of the  $\text{CH}_4$  background signal. For  $\text{XCH}_4$  the stratospheric and the tropospheric backgrounds have to be removed, whereas only the tropospheric background has to be removed for  $\text{TXCH}_4$ . Despite this difference, we estimate very similar emission rates from both data sets, and the emission rate uncertainties of using  $\text{XCH}_4$  or  $\text{TXCH}_4$  are small compared to the estimated emission rates.

Figure 8 summarizes the estimated emission strengths derived from different products based on different a priori knowledge of inventories and wind information at different altitudes (for specific values see Table A1). Different a priori inventories result in 16%–32% changes in strength at different altitudes, which is generally smaller than the 47% difference in the total amount of inventories ( $9.7 \times 10^{26}$  for CAMS-GLOB-ANT and  $6.6 \times 10^{26} \text{ molec. s}^{-1}$  for CoMet inventory). This is probably due to the different locations of sources and different proportions of each emission source in the total strengths in the two inventories. When using the CAMS-GLOB-ANT inventory,  $\text{CH}_4$  emission rates derived from CAMS  $\text{XCH}_4$  and  $\text{TXCH}_4$  are  $\sim 37\%$  and  $\sim 56\%$  higher than those derived from TROPOMI  $\text{XCH}_4$  and IASI + TROPOMI  $\text{TXCH}_4$ , respectively. This difference is mainly due to the difference between the CAMS forecast and satellite products. The strength increases with respect to the increasing wind speed at higher altitude, while the increment is not always proportional to the wind speed, i.e., less increase in the strength with respect to the wind speed at higher altitude (see Sect. 3.3.1).

### 3.3 Uncertainty analysis

The  $\text{CH}_4$  signal is weak compared to the background concentration which shows an increasing trend with obvious seasonality and strong day-to-day signals. It is necessary to remove the background signals before estimating the emission strengths. However, the imperfect elimination of the back-





**Figure 7.** Similar to Fig. 5, but for TROPOMI XCH<sub>4</sub> (a–c) and TROPOMI + IASI TXCH<sub>4</sub> (d–f). The a priori knowledge of sources are based on the CoMet inventory ( $6.6 \times 10^{26}$  molec. s<sup>-1</sup> in total, Gałkowski et al., 2021a). The triangle symbols represent the locations of the active coal mine shafts and different colors denote the amount of emission rates.

ground introduces uncertainties, which can be determined by considering the deficits of the background model and the noise in the background (Tu et al., 2022). In this study, the uncertainties of the estimated strengths include the background uncertainties.

Winds, particularly near the surface, are significantly altered by topography, which yields uncertainties in knowing the transport pathway from emission sources to the measurement location (Chen et al., 2016; Babenhauserheide et al., 2020). Thus, wind is one of the most important factors in correctly estimating the emission rates. Here, we investigate the wind uncertainties based on the CAMS XCH<sub>4</sub> and the CAMS-GLOB-ANT inventory. The wind used in Sect. 3.3.2 and 3.3.3 are from ERA5 at 10 m.

### 3.3.1 Vertical wind shear

Compared to the wind at 330 m, the distributions of wind directions are similar at lower or higher altitudes (10 and 500 m) but the wind speed increases with higher altitude (Fig. 3). The wind speed at 10 m is 20 % weaker than that at 330 m (Table 1), which yields a corresponding lower emission estimate of  $613 \pm 13$  kt yr<sup>-1</sup> ( $7.3 \times 10^{26} \pm 1.5 \times 10^{25}$  molec. s<sup>-1</sup>, -25 %) based on the CAMS XCH<sub>4</sub> and CAMS emission inventory (Fig. A4a).

Assuming that the height of the planetary boundary layer (PBL) is typically less than a kilometer, we use the ERA5 wind at 500 m above the ground (Fig. 3c) for describing

the transport of CH<sub>4</sub> released in the study region. The wind speed at 500 m increases by 22 % and 37 % for NE and SW regimes, respectively, i.e., 32 % on average, compared to the wind at 330 m. The share of SW directed winds is slightly larger at the 500 m level. These differences result in an increase of 13 % of the estimated emission rate ( $924 \pm 19$  kt yr<sup>-1</sup>,  $1.1 \times 10^{27} \pm 2.3 \times 10^{25}$  molec. s<sup>-1</sup>). The wind speed is linear in the calculation of  $\varepsilon$  (Eq. 2), but the wind speeds do not all linearly change for each grid and for each time at different levels. This results in unequal changes between the wind speed and the enhanced columns, and later unequal changes in the estimated emission strength. In addition, the simple cone plume model introduces biases, i.e., the enhanced column in the downwind is set to zero when its location is out of the cone angle (60°). Slight changes in the wind directions might result in a huge difference in the enhanced columns.

### 3.3.2 Use of narrowed angular wind regimes

The long-term wind comes from all directions (0–360°) (Fig. 3). To define the uncertainty of wind regimes' coverage, the wind is separated into two groups with narrow coverage fields: NE<sub>1/4</sub> (0–90°)–SW<sub>1/4</sub> (180–270°) and NW<sub>1/4</sub> (270–360°)–SE<sub>1/4</sub> (90–180°). The final estimated emission strength is weighted by the number of days on which, on average, the wind blew in the respective wind regime (i.e., 115 d for NE<sub>1/4</sub>–SW<sub>1/4</sub> and 71 d for NW<sub>1/4</sub>–SE<sub>1/4</sub>, respec-

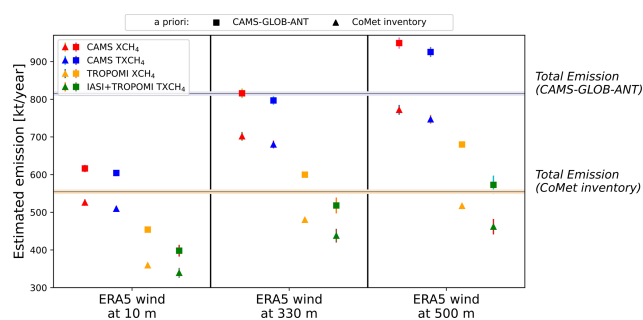


**Figure 8.** Estimated CH<sub>4</sub> emission rates derived from the CAMS forecasts (XCH<sub>4</sub> and TXCH<sub>4</sub>), TROPOMI XCH<sub>4</sub>, and TROPOMI + IASI TXCH<sub>4</sub> data based on different a priori knowledge of emission sources (CAMS-GLOB-ANT and CoMet inventories) and on ERA5 model winds at different altitudes (10, 330, 500 m). Square symbols represent the a priori emission sources from the CAMS-GLOB-ANT inventory and triangle symbols represent the a priori emission sources from the CoMet inventory. The two horizontal lines represent the number of total emissions for the CAMS-GLOB-ANT inventory (lavender color) and for the CoMet inventory (orange color), respectively. Note that error bars represent the uncertainties from background removal and noise in the data, which are much smaller than the results and they are not visible here. For specific values see Table A1.

tively). The XCH<sub>4</sub> anomalies and the plume for the NE<sub>1/4</sub>–SW<sub>1/4</sub> regime are quite similar to those with wider-coverage NE and SW fields (Fig. 9a–c). The wind-assigned anomalies derived from CAMS and the simple cone plume model show very good agreement as well. Slightly less data points are found here because of the choice of narrower wind fields, especially for NW<sub>1/4</sub>–SE<sub>1/4</sub> wind fields. The estimated emission rate is about  $773 \pm 19 \text{ kt yr}^{-1}$  ( $9.2 \times 10^{26} \pm 2.3 \times 10^{25} \text{ molec. s}^{-1}$ ) for the NE<sub>1/4</sub>–SW<sub>1/4</sub> field. This indicates that the effect of the segment in the wind field coverage is negligible when there are enough measurements. The use of NW<sub>1/4</sub>–SE<sub>1/4</sub> wind fields yields an emission strength of  $1176 \pm 134 \text{ kt yr}^{-1}$  ( $1.4 \times 10^{27} \pm 1.6 \times 10^{26} \text{ molec. s}^{-1}$ ). The higher uncertainty is probably due to less measurements in these wind fields. The weighted rate is therefore about  $927 \text{ kt yr}^{-1}$  ( $1.1 \times 10^{27} \text{ molec. s}^{-1}$ ), 13.4 % higher than based on the wider NE–SW wind regime (Sect. 3.1).

### 3.3.3 Investigation of different choices for wind field segmentation

The wind category here is based on the predominant wind fields over the USCB region and is divided into two opposite regimes (SW and NE). To investigate the effect of the segmentation on the uncertainty in the emission rate estimation, we additionally apply another kind of segmentation: N ( $< 90^\circ$  or  $> 270^\circ$ ) and S ( $90$ – $270^\circ$ ) categories. Similar results are found and are shown in Fig. 10. Though the 2D distribution of the plume changes due to the new wind category, an obvious plume can be seen. The estimated emission rate is

$773 \pm 19 \text{ kt yr}^{-1}$  ( $9.2 \times 10^{26} \pm 2.3 \times 10^{25} \text{ molec. s}^{-1}$ ), which is only 5.2 % less than that using NE and SW wind categories. The correlation of the wind-assigned anomalies derived from the CAMS and the simple cone plume model shows a very good agreement as well, with a similar  $R^2$  value of 0.85 to that in the NE–SW wind category. This result demonstrates that our method is not significantly influenced by the wind regime division.

### 3.3.4 Investigation of different choices for angle of the emission cone

The angle ( $\alpha = 60^\circ$ ) used in the simple cone plume model is an empirical value which affects the deduced emission strengths. Figure 11 shows the results when  $\alpha$  is decreased or increased by  $10^\circ$ . Changes in the spatial distributions of wind-assigned anomalies and in the correlations derived from CAMS and the simple cone plume model are nearly negligible when using different angles in the model. The estimated emissions are  $789 \pm 16 \text{ kt a}^{-1}$  ( $9.5 \times 10^{26} \pm 1.9 \times 10^{25} \text{ molec. s}^{-1}$ ) for  $\alpha = 50^\circ$  and  $832 \pm 17 \text{ kt a}^{-1}$  ( $9.9 \times 10^{26} \pm 2.0 \times 10^{25} \text{ molec. s}^{-1}$ ) for  $\alpha = 70^\circ$ , which are 3 % lower and 2 % higher than that using the empirical angle ( $\alpha = 60^\circ$ ).

The changes in the estimated emission rates for different products due to different error sources are summarized in Table A2. Based on the error propagation, the total uncertainty in the estimated emission rates from the different error sources (background removal and noise in the data, vertical wind shear at 500 m, wind field segmentation, and opening angle  $\alpha = 70^\circ$ ) is approximately 14.7 % for CAMS XCH<sub>4</sub>, 14.8 % for TROPOMI XCH<sub>4</sub>, and 11.4 % for TROPOMI + IASI TXCH<sub>4</sub>. Note that the use of narrowed angular wind regimes is not a preferable way due to few amounts of data in narrowed wind regimes, and thus is not considered an error source. In addition, the 500 m wind shear was used as a contribution to the budget, as the 10 m wind is not expected to be representative of the PBL.

## 4 Conclusions

Intensive mining activities are the dominant CH<sub>4</sub> emission sources in the USCB region, Poland, where one of the largest coal mining areas in Europe is located. It is thus of importance to quantify the CH<sub>4</sub> emissions from this area. In this study we use the combination of a simple cone plume model and a novel wind-assigned model to estimate CH<sub>4</sub> emission rates from high-resolution CAMS forecast XCH<sub>4</sub> and TXCH<sub>4</sub>, along with satellite data (TROPOMI XCH<sub>4</sub> and TROPOMI+IASI TXCH<sub>4</sub>) over the USCB region (49.3–50.8° N and 18–20° E) from November 2017 to December 2020.

Based on the CAMS-GLOB-ANT inventory, the dominant CH<sub>4</sub> source is emitted from energy production and distribution, and the significant sources are spread around the

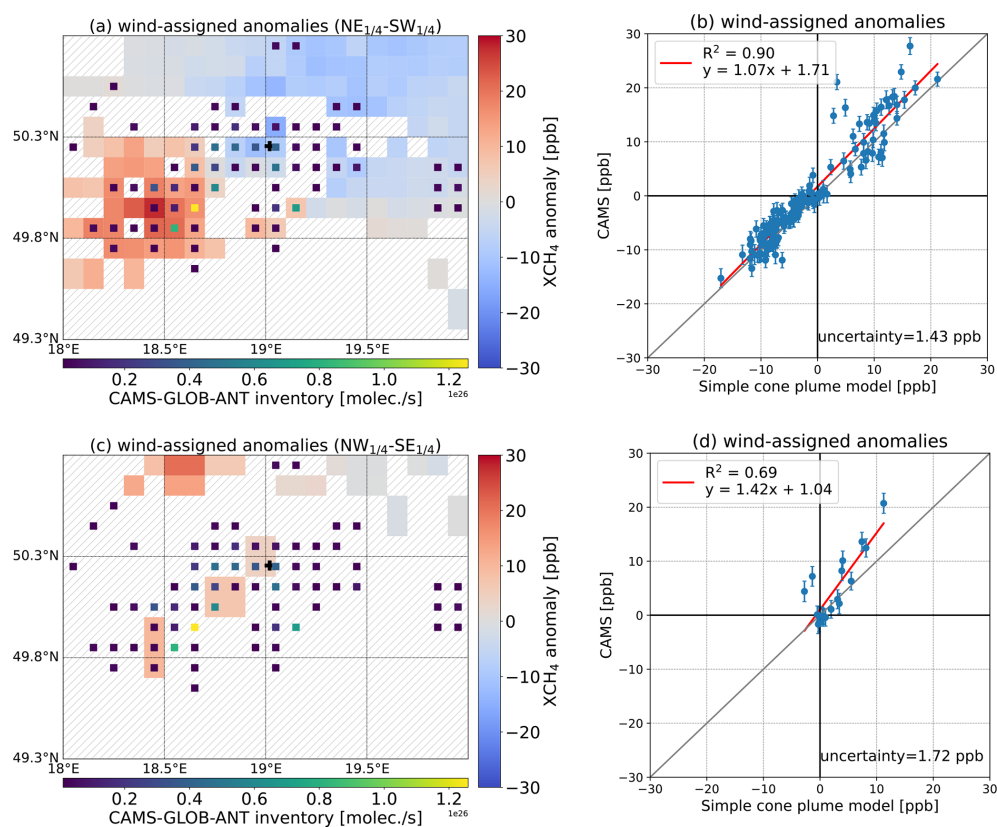


**Figure 9.** Similar figures to Fig. 5b–c. Results are derived from CAMS XCH<sub>4</sub>, CAMS emission inventory and ERA5 wind at 330 m for (a)–(b) narrow wind coverage (NE<sub>1/4</sub> and SW<sub>1/4</sub>), and (c)–(d) narrow wind coverage (NW<sub>1/4</sub> and SE<sub>1/4</sub>).

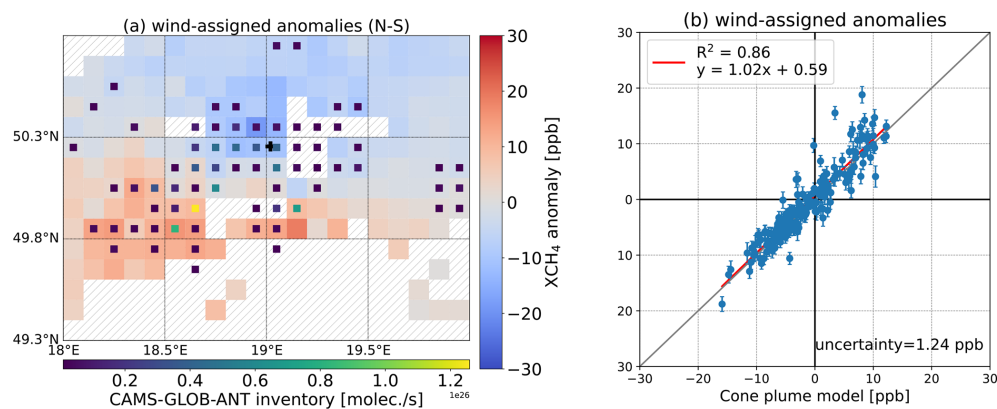


**Figure 10.** Similar figures to Fig. 5b–c. Results are derived from CAMS XCH<sub>4</sub>, CAMS emission inventory and ERA5 wind at 330 m, but using a new wind category (N and S).

city of Katowice and its southwest region. We firstly apply the wind-assigned method to the CAMS forecasts based on the a priori knowledge of the CAMS-GLOB-ANT inventory (815 kt yr<sup>-1</sup>,  $9.7 \times 10^{26}$  molec. s<sup>-1</sup> in total) and ERA5 wind at  $\sim 330$  m. We use the wind-assigned anomalies of XCH<sub>4</sub>/TXCH<sub>4</sub> to represent the difference of XCH<sub>4</sub>/TXCH<sub>4</sub> between the conditions of two opposite wind fields (NE and SW). The wind-assigned anomalies derived from CAMS

XCH<sub>4</sub>/TXCH<sub>4</sub> show very good agreements with the output of the simple cone plume model with an  $R^2$  value of 0.85 for CAMS XCH<sub>4</sub> and CAMS TXCH<sub>4</sub>. This nice correlation indicates that our background removal works well. In addition, similar estimates are derived from CAMS XCH<sub>4</sub> (815 kt yr<sup>-1</sup>, i.e.,  $9.7 \times 10^{26}$  molec. s<sup>-1</sup>) and TXCH<sub>4</sub> (798 kt yr<sup>-1</sup>, i.e.,  $9.5 \times 10^{26}$  molec. s<sup>-1</sup>).

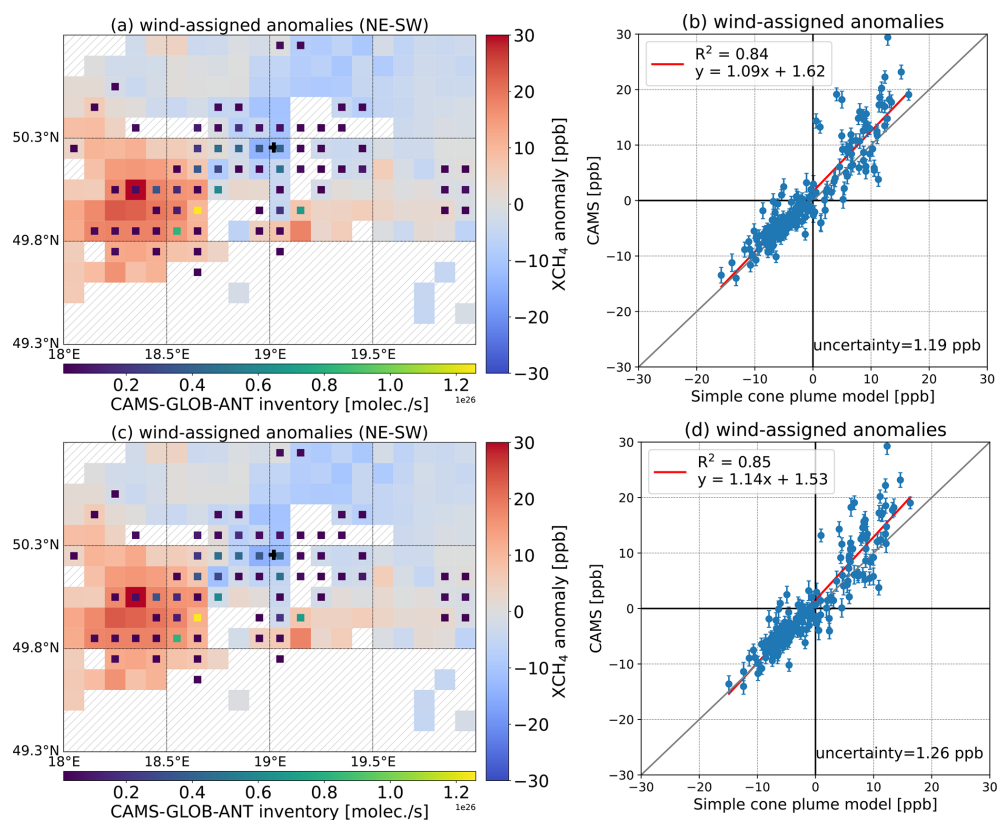


**Figure 11.** Similar figures to Fig. 5b–c. Results are derived from CAMS XCH<sub>4</sub>, CAMS emission inventory, and ERA5 wind at 330 m for (a)–(b)  $\alpha = 50^\circ$ , and (c)–(d)  $\alpha = 70^\circ$ .

To investigate the CH<sub>4</sub> emissions from this hot spot, the CoMet campaign was performed in 2018. Locations and emission rates of the ventilation shafts of the coal mine used in this study are based on this campaign. Based on this knowledge, the emissions are estimated as  $496 \text{ kt yr}^{-1}$  ( $5.9 \times 10^{26} \text{ molec. s}^{-1}$ ) and  $437 \text{ kt yr}^{-1}$  ( $5.2 \times 10^{26} \text{ molec. s}^{-1}$ ) from the TROPOMI XCH<sub>4</sub> and combined TROPOMI + IASI TXCH<sub>4</sub>, respectively. These results are 40 % less than that derived from the CAMS model and CAMS-GLOB-ANT inventory. It is probably because CAMS-GLOB-ANT includes many sectors of anthropogenic sources, like wastes, and residential and commercial combustion, which account for about 20 %. Nevertheless, our results derived from satellite observations are close to the E-PRTR inventory of  $448 \text{ kt yr}^{-1}$  and reasonable compared to the CoMet inventory ( $555 \text{ kt yr}^{-1}$ ), and to previous studies over the USCB region (ranging from 9 to  $79 \text{ kt yr}^{-1}$  for a sub-cluster of shafts (Krautwurst et al., 2021) up to  $477 \text{ kt yr}^{-1}$  derived from one flight (Fiehn et al., 2020)).

Similar 2D anomalies and plumes are also observed for TROPOMI XCH<sub>4</sub> and TROPOMI + IASI TXCH<sub>4</sub>. This nicely documents the robustness of the method. The TROPOMI + IASI result has a higher uncertainty than the TROPOMI result, because (1) the vertical distribution of CH<sub>4</sub> is in general much more difficult to measure than the

total column of CH<sub>4</sub> and (2) the vertical distribution is derived by considering two independent measurements, each with its own noise error. This might change for a larger number of data points (e.g., by using data from more years or by applying the method to IASI and TROPOMI successors on the upcoming METOP-SG satellite, which offers much more collocated observations). Nonetheless, the uncertainties are insignificant compared to the estimated emission rates.

Wind contains uncertainties in knowing the transport pathway from emission sources to the measurement location and thus, we analyze the effects in selecting wind at lower and higher altitudes (10 and 500 m), wind field coverage, and wind category. Wind distributions at higher levels are similar to the ones at 330 m. However, their speeds decrease by 20 % at 10 m and increase by 32 % at 500 m, which results in changes in the emission rates by  $-25 \%$  and  $13 \%$  for CAMS XCH<sub>4</sub>, respectively. Narrower wind field coverage ( $0\text{--}90^\circ$  for the NE regime and  $180\text{--}270^\circ$  for the SW regime) and different wind segmentation ( $< 90^\circ$  or  $> 270^\circ$  for N regime and  $90\text{--}270^\circ$  for S regime) introduce uncertainties of  $+13.4 \%$  and  $-5.2 \%$  for CAMS XCH<sub>4</sub>, respectively. The agreements for these sensitivity tests of the wind-assigned anomalies derived from both the CAMS and simple cone plume models are as good as that using previous NE and SW wind fields. The impact of a suboptimal choice for the angle ( $60^\circ$ ) used

in the simple cone plume model is also discussed. The estimation is decreased by 3 % for  $\alpha = 50^\circ$  and increased by 2 % for  $\alpha = 70^\circ$  for CAMS XCH<sub>4</sub>. This small change supports the empirical choice for  $\alpha$ . Based on the error propagation, the total uncertainty in the estimated emission rates from the different error sources (background removal and noise in the data, vertical wind shear at 500 m, wind field segmentation, and opening angle  $\alpha = 70^\circ$ ) is approximately 14.7 % for CAMS XCH<sub>4</sub>, 14.8 % for TROPOMI XCH<sub>4</sub>, and 11.4 % for TROPOMI+IASI TXCH<sub>4</sub>. These results suggest that the wind-assigned method is robust and is also suitable for estimating CH<sub>4</sub> and CO<sub>2</sub> emissions in other regions.

## Appendix A

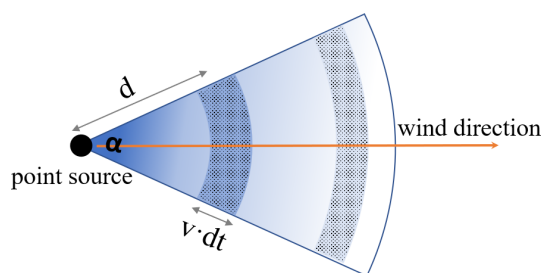


**Figure A1.** Sketch of the simple cone plume model used to explain the CH<sub>4</sub> emission estimation method. The CH<sub>4</sub> at the point source is distributed along the wind direction (wind speed:  $v$ ) in the cone-shaped area with an opening angle of  $\alpha$ . The point source emits the CH<sub>4</sub> at an emission rate of  $\varepsilon$ . We assumed the CH<sub>4</sub> molecules are evenly distributed in the dotted area A, and the distance from area A to the point source is  $d$ . Therefore, the emitted CH<sub>4</sub> in  $dt$  time period equals the amount of CH<sub>4</sub> in the area A. It yields the equation:  $\varepsilon \times dt \approx \Delta \text{column} \times \frac{\alpha}{\pi} \times \pi \times d \times v \times dt$ . This figure is adopted from Tu et al. (2022).

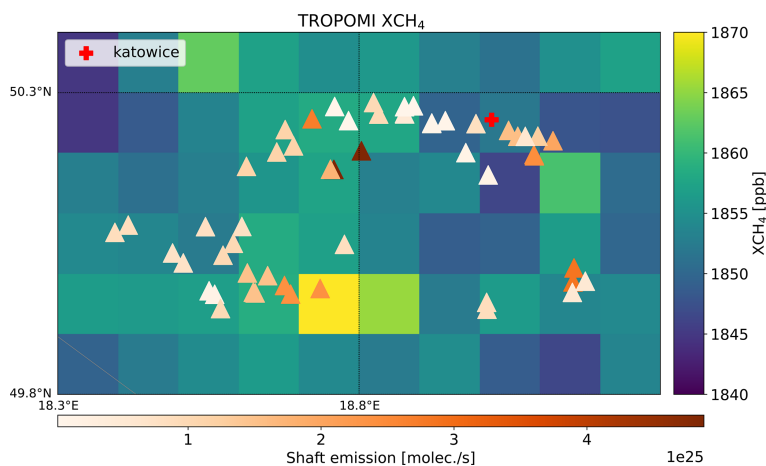


**Figure A2.** A zoomed figure of Fig. 4b.

**Table A1.** Estimated CH<sub>4</sub> emission rates derived from CAMS forecasts (XCH<sub>4</sub> and TXCH<sub>4</sub>), TROPOMI XCH<sub>4</sub>, and IASI & TROPOMI TXCH<sub>4</sub> data based on different a priori knowledge of emission sources (CAMS-GLOB-ANT and CoMet campaign inventories) and ERA5 model winds at different altitudes (10, 100 and ~500 m).

	ERA5 wind at 10 m		ERA5 wind at 330 m (975 hPa)		ERA5 wind at 500 m (950 hPa)	
	CAMS-GLOB-ANT (total = prior emission sources)	CoMet inventory (total =)	CAMS-GLOB-ANT (total =)	CoMet inventory (total =)	CAMS-GLOB-ANT (total =)	CoMet inventory (total =)
CAMS XCH <sub>4</sub>	$7.3 \times 10^{26} \pm 1.5 \times 10^{25}$	$6.3 \times 10^{26} \pm 1.3 \times 10^{25}$	$9.7 \times 10^{26} \pm 2.0 \times 10^{25}$	$8.3 \times 10^{26} \pm 1.8 \times 10^{25}$	$1.1 \times 10^{27} \pm 2.3 \times 10^{25}$	$9.2 \times 10^{26} \pm 2.1 \times 10^{25}$
CAMS TXCH <sub>4</sub>	$7.2 \times 10^{26} \pm 1.3 \times 10^{25}$	$6.1 \times 10^{26} \pm 1.2 \times 10^{25}$	$9.5 \times 10^{26} \pm 1.8 \times 10^{25}$	$8.1 \times 10^{26} \pm 1.6 \times 10^{25}$	$1.0 \times 10^{27} \pm 2.1 \times 10^{25}$	$8.9 \times 10^{26} \pm 1.9 \times 10^{25}$
TROPOMI XCH <sub>4</sub>	$5.4 \times 10^{26} \pm 1.8 \times 10^{25}$	$4.5 \times 10^{26} \pm 1.5 \times 10^{25}$	$7.1 \times 10^{26} \pm 2.4 \times 10^{25}$	$5.9 \times 10^{26} \pm 2.1 \times 10^{25}$	$8.1 \times 10^{26} \pm 2.8 \times 10^{25}$	$6.3 \times 10^{26} \pm 2.3 \times 10^{25}$
IASI&TROPOMI TXCH <sub>4</sub>	$4.7 \times 10^{26} \pm 2.7 \times 10^{25}$	$4.0 \times 10^{26} \pm 2.3 \times 10^{25}$	$6.2 \times 10^{26} \pm 3.7 \times 10^{25}$	$5.2 \times 10^{26} \pm 3.2 \times 10^{25}$	$6.8 \times 10^{26} \pm 4.3 \times 10^{25}$	$5.5 \times 10^{26} \pm 3.6 \times 10^{25}$

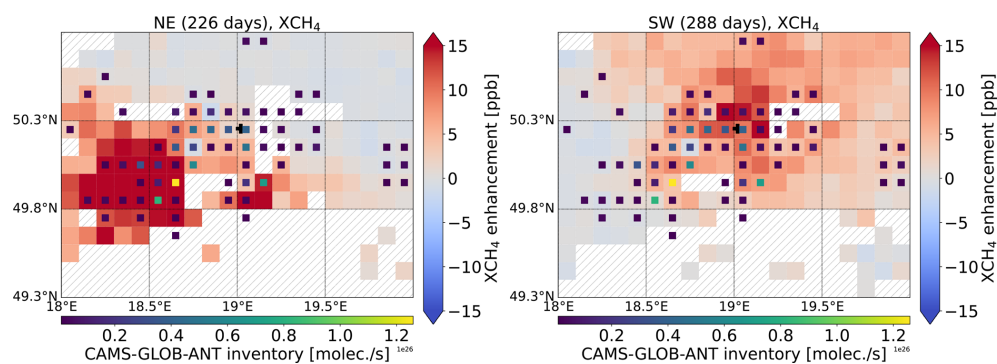


**Figure A3.** The enhancements for wind coming from NE and SW.

**Table A2.** Changes in the estimated emission rates for different products when using different input data or under different situations compared to their results using the default setting (wind at 330 m, NE–SW wind segmentation,  $\alpha = 60^\circ$ , CAMS-GLOB-ANT for CAMS XCH<sub>4</sub> and CoMet inventory for TROPOMI XCH<sub>4</sub> and TROPOMI + IASI TXCH<sub>4</sub>).

	CAMS XCH <sub>4</sub>	TROPOMI XCH <sub>4</sub>	TROPOMI + IASI TXCH <sub>4</sub>
Background removal & noise in the data	2.1 %	3.6 %	6.1 %
Vertical wind shear (500 m)	13.4 %	6.8 %	5.8 %
Wind field segmentation (N–S)	−5.2 %	12.7 %	7.7 %
Angle of the emission cone ( $\alpha = 70^\circ$ )	2.1 %	0.07 %	−0.02 %
Total:	14.7 %	14.8 %	11.4 %

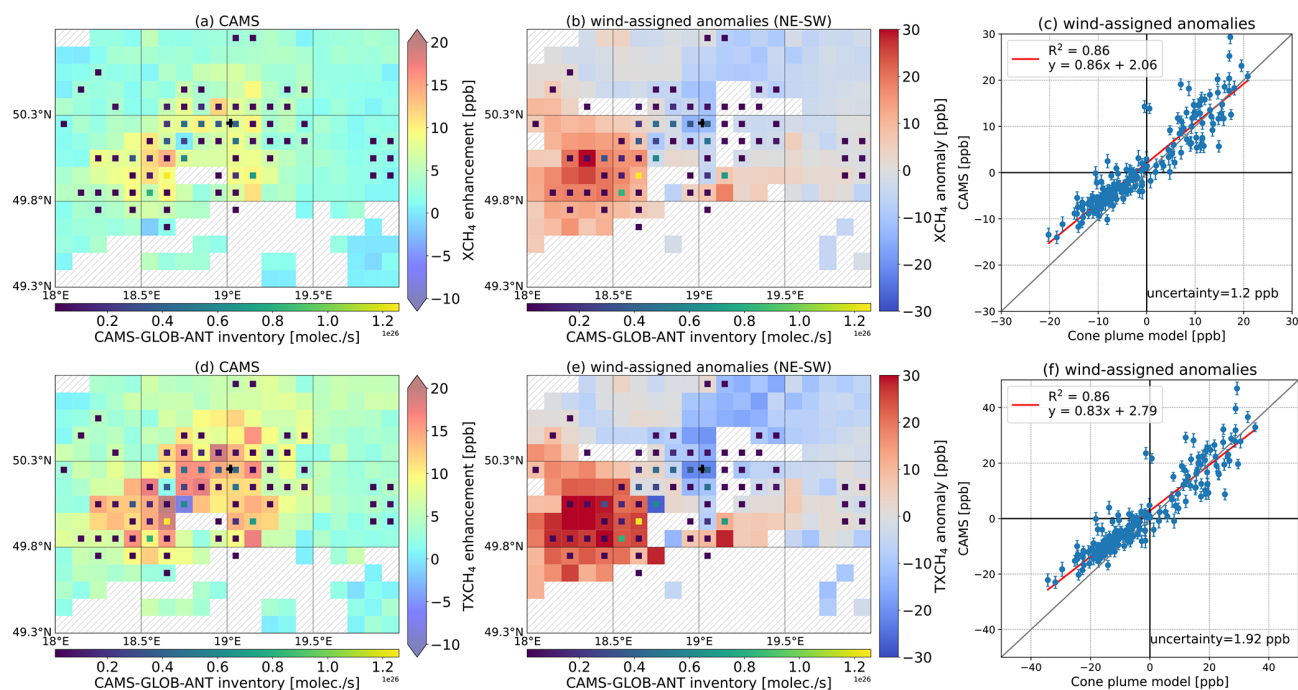


**Figure A4.** Similar to Fig. 5 but using ERA5 wind at 10 m.

**Data availability.** The data are accessible by contacting the corresponding author (qiansi.tu@kit.edu). The SRON S5P-RemoTeC scientific TROPOMI CH<sub>4</sub> data set from this study is available for download at <https://doi.org/10.5281/zenodo.4447228> (Lorente et al., 2021b). The MUSICA IASI data set is available for download via <https://doi.org/10.35097/408> (Schneider et al., 2021). The CoMet inventory is available at <https://doi.org/10.18160/3K6Z-4H73> (Gałkowski et al., 2021a).

**Author contributions.** QT, FH and MS developed the research question. QT wrote the manuscript and performed the data analysis with input from FH, MS and FK. MS, BE and CJD provided the combined (MUSICA IASI + TROPOMI) data and supported technically for the analysis of these data. JN supported consultation of the local situation and CoMet inventory. All authors discussed the results and contributed to the final manuscript.

**Competing interests.** At least one of the (co-)authors is a member of the editorial board of *Atmospheric Chemistry and Physics*. The peer-review process was guided by an independent editor, and the authors also have no other competing interests to declare.

**Disclaimer.** Publisher's note: Copernicus Publications remains neutral with regard to jurisdictional claims in published maps and institutional affiliations.

**Special issue statement.** This article is part of the special issue "CoMet: a mission to improve our understanding and to better quantify the carbon dioxide and methane cycles". It is not associated with a conference.

**Acknowledgements.** The CAMS results were generated using the Copernicus Atmosphere Monitoring Service (2017–2020) information. Neither the European Commission nor ECMWF is responsible for any use that may be made of the Copernicus information or data it contains. We also thank Michela Giusti and Kevin Marsh in the Data Support Team at ECMWF for retrieving and providing comments about the CAMS data. This research has largely benefited from funds of the Deutsche Forschungsgemeinschaft (provided for the two projects MOTIV and TEDDY with IDs 290612604 and 416767181, respectively). An important part of this work was performed on the supercomputer, HoreKa, funded by the Ministry of Science, Research and the Arts Baden-Württemberg and by the German Federal Ministry of Education and Research. We acknowledge Emissions of atmospheric Compounds and Compilation of Ancillary Data (ECCAD) for providing CAMS-GLOB-ANT inventory data. We also give thanks to Claire Granier from Laboratoire d'Aerologie, Toulouse, France for providing information about the uncertainties of the CAMS-GLOB-ANT inventory. The access and use of any Copernicus Sentinel data available through the Copernicus Open Access Hub are governed by the legal notice on the use of Copernicus Sentinel Data and Service Information, which is given here: <https://sentinels.copernicus.eu/>

documents/247904/690755/Sentinel\_Data\_Legal\_Notice (last access: 8 November 2021).

We acknowledge the support by the Deutsche Forschungsgemeinschaft and the Open Access Publishing Fund of the Karlsruhe Institute of Technology.

**Financial support.** This research has been supported by the Deutsche Forschungsgemeinschaft (Project MOTIV (grant no. 290612604) and Project TEDDY (grant no. 416767181)). The Ministerium für Wissenschaft, Forschung und Kunst Baden-Württemberg and the Bundesministerium für Bildung und Forschung provided funds for the supercomputer HoreKa used for the MUSICA IASI retrieval work and the MUSICA IASI + TROPOMI combination calculations.

The article processing charges for this open-access publication were covered by the Karlsruhe Institute of Technology (KIT).

**Review statement.** This paper was edited by Christoph Gerbig and reviewed by two anonymous referees.

## References

- Agustí-Panareda, A., Diamantakis, M., Massart, S., Chevallier, F., Muñoz-Sabater, J., Barré, J., Curcoll, R., Engelen, R., Lange-rock, B., Law, R. M., Loh, Z., Morguá, J. A., Parrington, M., Peuch, V.-H., Ramonet, M., Roehl, C., Vermeulen, A. T., Warneke, T., and Wunch, D.: Modelling CO<sub>2</sub> weather – why horizontal resolution matters, *Atmos. Chem. Phys.*, 19, 7347–7376, <https://doi.org/10.5194/acp-19-7347-2019>, 2019.
- Andersen, T., Vinkovic, K., de Vries, M., Kers, B., Necki, J., Swolkien, J., Roiger, A., Peters, W., and Chen, H.: Quantifying methane emissions from coal mining ventilation shafts using an unmanned aerial vehicle (UAV)-based active AirCore system, *Atmos. Environ.*, 12, 100135, <https://doi.org/10.1016/j.aeaoa.2021.100135>, 2021.
- Babenhauerheide, A., Hase, F., and Morino, I.: Net CO<sub>2</sub> fossil fuel emissions of Tokyo estimated directly from measurements of the Tsukuba TCCON site and radiosondes, *Atmos. Meas. Tech.*, 13, 2697–2710, <https://doi.org/10.5194/amt-13-2697-2020>, 2020.
- Barré, J., Aben, I., Agustí-Panareda, A., Balsamo, G., Bousserez, N., Dueben, P., Engelen, R., Inness, A., Lorente, A., McNorton, J., Peuch, V.-H., Radnoti, G., and Ribas, R.: Systematic detection of local CH<sub>4</sub> anomalies by combining satellite measurements with high-resolution forecasts, *Atmos. Chem. Phys.*, 21, 5117–5136, <https://doi.org/10.5194/acp-21-5117-2021>, 2021.
- Boesch, H., Baker, D., Connor, B., Crisp, D., and Miller, C.: Global Characterization of CO<sub>2</sub> Column Retrievals from Shortwave-Infrared Satellite Observations of the Orbiting Carbon Observatory-2 Mission, *Remote Sens.*, 3, 270–304, <https://doi.org/10.3390/rs3020270>, 2011.
- Butz, A., Hasekamp, O. P., Frankenberg, C., and Aben, I.: Retrievals of atmospheric CO<sub>2</sub> from simulated space-borne measurements of backscattered near-infrared sunlight: accounting for aerosol effects, *Appl. Opt.* 48, 3322–3336, 2009.



- Butz, A., Guerlet, S., Hasekamp, O., Schepers, D., Galli, A., Aben, I., Frankenberg, C., Hartmann, J.-M., Tran, H., Kuze, A., Keppel-Aleks, G., Toon, G., Wunch, D., Wennberg, P., Deutscher, N., Griffith, D., Macatangay, R., Messerschmidt, J., Notholt, J., and Warneke, T.: Toward accurate CO<sub>2</sub> and CH<sub>4</sub> observations from GOSAT, *Geophys. Res. Lett.*, 38, L14812, <https://doi.org/10.1029/2011GL047888>, 2011.
- Chen, J., Viatte, C., Hedelius, J. K., Jones, T., Franklin, J. E., Parker, H., Gottlieb, E. W., Wennberg, P. O., Dubey, M. K., and Wofsy, S. C.: Differential column measurements using compact solar-tracking spectrometers, *Atmos. Chem. Phys.*, 16, 8479–8498, <https://doi.org/10.5194/acp-16-8479-2016>, 2016.
- Collard, A. D.: Selection of IASI Channels for Use in Numerical Weather Prediction, ECMWF, <https://www.ecmwf.int/node/8760> (last access: 12 July 2022), 2007.
- Coopmann, O., Guidard, V., Fourrié, N., Josse, B., and Maréchal, V.: Update of Infrared Atmospheric Sounding Interferometer (IASI) channel selection with correlated observation errors for numerical weather prediction (NWP), *Atmos. Meas. Tech.*, 13, 2659–2680, <https://doi.org/10.5194/amt-13-2659-2020>, 2020.
- Copernicus Climate Change Service (C3S): ERA5: Fifth generation of ECMWF atmospheric reanalyses of the global climate. Copernicus Climate Change Service Climate Data Store (CDS), <https://cds.climate.copernicus.eu/cdsapp#!/home> (last access: 12 July 2022), 2017.
- Crippa, M., Guizzardi, D., Muntean, M., Schaaf, E., Dentener, F., van Aardenne, J. A., Monni, S., Doering, U., Olivier, J. G. J., Pagliari, V., and Janssens-Maenhout, G.: Gridded emissions of air pollutants for the period 1970–2012 within EDGAR v4.3.2, *Earth Syst. Sci. Data*, 10, 1987–2013, <https://doi.org/10.5194/essd-10-1987-2018>, 2018.
- Diekmann, C. J., Schneider, M., Ertl, B., Hase, F., García, O., Khosrawi, F., Sepúlveda, E., Knippertz, P., and Braesicke, P.: The global and multi-annual MUSICA IASI {H<sub>2</sub>O, δD} pair dataset, *Earth Syst. Sci. Data*, 13, 5273–5292, <https://doi.org/10.5194/essd-13-5273-2021>, 2021.
- Fiehn, A., Kostinek, J., Eckl, M., Klausner, T., Gałkowski, M., Chen, J., Gerbig, C., Röckmann, T., Maazallahi, H., Schmidt, M., Korbeň, P., Nečki, J., Jagoda, P., Wildmann, N., Mallaun, C., Bun, R., Nickl, A.-L., Jöckel, P., Fix, A., and Roiger, A.: Estimating CH<sub>4</sub>, CO<sub>2</sub> and CO emissions from coal mining and industrial activities in the Upper Silesian Coal Basin using an aircraft-based mass balance approach, *Atmos. Chem. Phys.*, 20, 12675–12695, <https://doi.org/10.5194/acp-20-12675-2020>, 2020.
- Flemming, J., Huijnen, V., Arteta, J., Bechtold, P., Beljaars, A., Blechschmidt, A.-M., Diamantakis, M., Engelen, R. J., Gaudel, A., Inness, A., Jones, L., Josse, B., Katragkou, E., Marecal, V., Peuch, V.-H., Richter, A., Schultz, M. G., Stein, O., and Tsikerdekis, A.: Tropospheric chemistry in the Integrated Forecasting System of ECMWF, *Geosci. Model Dev.*, 8, 975–1003, <https://doi.org/10.5194/gmd-8-975-2015>, 2015.
- De Gouw, J. A., Veeffkind, J. P., Roosenbrand, E., Dix, B., Lin, J. C., Landgraf, J., and Levelt, P. F.: Daily Satellite Observations of Methane from Oil and Gas Production Regions in the United States, *Sci. Rep.*, 10, 1379, <https://doi.org/10.1038/s41598-020-57678-4>, 2020.
- E-PRTR: The European Pollutant Release and Transfer Register (E-PRTR), Member States reporting under Article 7 of Regulation (EC) No. 166/2006, <https://www.eea.europa.eu/data-and-maps/data/member-states-reporting-art-7>, (last access: 12 July 2022), 2017.
- Gałkowski, M., Fiehn, A., Swolkien, J., Stanisavljevic, M., Korben, P., Menoud, M., Necki, J., Roiger, A., Röckmann, T., Gerbig, C., and Fix, A.: Emissions of CH<sub>4</sub> and CO<sub>2</sub> over the Upper Silesian Coal Basin (Poland) and its vicinity (4.01), ICOS ERIC – Carbon Portal [data set], <https://doi.org/10.18160/3K6Z-4H73>, 2021a.
- Gałkowski, M., Jordan, A., Rothe, M., Marshall, J., Koch, F.-T., Chen, J., Agusti-Panareda, A., Fix, A., and Gerbig, C.: In situ observations of greenhouse gases over Europe during the CoMet 1.0 campaign aboard the HALO aircraft, *Atmos. Meas. Tech.*, 14, 1525–1544, <https://doi.org/10.5194/amt-14-1525-2021>, 2021b.
- García, O. E., Schneider, M., Ertl, B., Sepúlveda, E., Borger, C., Diekmann, C., Wiegeler, A., Hase, F., Barthlott, S., Blumenstock, T., Raffalski, U., Gómez-Peláez, A., Steinbacher, M., Ries, L., and de Frutos, A. M.: The MUSICA IASI CH<sub>4</sub> and N<sub>2</sub>O products and their comparison to HIPPO, GAW and NDACC FTIR references, *Atmos. Meas. Tech.*, 11, 4171–4215, <https://doi.org/10.5194/amt-11-4171-2018>, 2018.
- Granier, C., Darras, S., Denier van der Gon, H., Doubalova, J., Elguindi, N., Galle, B., Gauss, M., Guevara, M., Jalkanen, J.-P., Kuenen, J., Liouise, C., Quack, B., Simpson, D., and Sindelarova, K.: The Copernicus Atmosphere Monitoring Service global and regional emissions (April 2019 version), Copernicus Atmosphere Monitoring Service (CAMS) report, <https://doi.org/10.24380/d0bn-kx16>, 2019.
- Hasekamp, O. P. and Butz, A.: Efficient calculation of intensity and polarization spectra in vertically inhomogeneous scattering and absorbing atmospheres, *J. Geophys. Res.*, 113, D20309, <https://doi.org/10.1029/2008JD010379>, 2008.
- Hasekamp, O., Lorente, A., Hu, H., Butz, A., van de Brugh, J., and Landgraf, J.: Algorithm Theoretical Baseline Document for Sentinel-5 Precursor methane retrieval, <http://www.tropomi.eu/sites/default/files/files/publicSentinel-5P-TROPOMI-ATBD-Methane-retrieval.pdf> (last access: 12 July 2022), 2019.
- Hersbach, H., Bell, B., Berrisford, P., Hirahara, S., Horányi, A., Muñoz-Sabater, J., Nicolas, J., Peubey, C., Radu, R., Schepers, D., Simmons, A., Soci, C., Abdalla, S., Abellan, X., Balsamo, G., Bechtold, P., Biavati, G., Bidlot, J., Bonavita, M., De Chiara, G., Dahlgren, P., Dee, D., Diamantakis, M., Dragani, R., Flemming, J., Forbes, R., Fuentes, M., Geer, A., Haimberger, L., Healy, S., Hogan, R. J., Hólm, E., Janisková, M., Keeley, S., Laloyaux, P., Lopez, P., Lupu, C., Radnoti, G., de Rosnay, P., Rozum, I., Vamborg, F., Villaume, S., and Thépaut, J.-N.: The ERA5 global reanalysis, *Q. J. Roy. Meteorol. Soc.*, 146, 1999–2049, <https://doi.org/10.1002/qj.3803>, 2020.
- Hoesly, R. M., Smith, S. J., Feng, L., Klimont, Z., Janssens-Maenhout, G., Pitkanen, T., Seibert, J. J., Vu, L., Andres, R. J., Bolt, R. M., Bond, T. C., Dawidowski, L., Kholod, N., Kurokawa, J.-I., Li, M., Liu, L., Lu, Z., Moura, M. C. P., O'Rourke, P. R., and Zhang, Q.: Historical (1750–2014) anthropogenic emissions of reactive gases and aerosols from the Community Emissions Data System (CEDS), *Geosci. Model Dev.*, 11, 369–408, <https://doi.org/10.5194/gmd-11-369-2018>, 2018.
- Kirschke, S., Bousquet, P., Ciais, P., Saunoy, M., Canadell, J. G., Dlugokencky, E. J., Bergamaschi, P., Bergmann, D., Blake, D. R., Bruhwiler, L., Cameron-Smith, P., Castaldi, S., Chevallier, F., Feng, L., Fraser, A., Heimann, M., Hodson, E. L., Houwel-

- ing, S., Josse, B., Fraser, P. J., Krummel, P. B., Lamarque, J.-F., Langenfelds, R. L., Le Quééré, C., Naik, V., O'Doherty, S., Palmer, P. I., Pison, I., Plummer, D., Poulter, B., Prinn, R. G., Rigby, M., Ringeval, B., Santini, M., Schmidt, M., Shindell, D. T., Simpson, I. J., Spahni, R., Steele, L. P., Strode, S. A., Sudo, K., Szopa, S., van der Werf, G. R., Voulgarakis, A., van Weele, M., Weiss, R. F., Williams, J. E., and Zeng, G.: Three decades of global methane sources and sinks, *Nat. Geosci.*, 6, 813–823, <https://doi.org/10.1038/ngeo1955>, 2013.
- Kostinek, J., Roiger, A., Eckl, M., Fiehn, A., Luther, A., Wildmann, N., Klausner, T., Fix, A., Knote, C., Stohl, A., and Butz, A.: Estimating Upper Silesian coal mine methane emissions from airborne in situ observations and dispersion modeling, *Atmos. Chem. Phys.*, 21, 8791–8807, <https://doi.org/10.5194/acp-21-8791-2021>, 2021.
- Krautwurst, S., Gerilowski, K., Borchardt, J., Wildmann, N., Gałkowski, M., Swolkień, J., Marshall, J., Fiehn, A., Roiger, A., Ruhtz, T., Gerbig, C., Necki, J., Burrows, J. P., Fix, A., and Bovensmann, H.: Quantification of CH<sub>4</sub> coal mining emissions in Upper Silesia by passive airborne remote sensing observations with the Methane Airborne MAPper (MAMAP) instrument during the CO<sub>2</sub> and Methane (CoMet) campaign, *Atmos. Chem. Phys.*, 21, 17345–17371, <https://doi.org/10.5194/acp-21-17345-2021>, 2021.
- Liu, M., van der A, R., van Weele, M., Eskes, H., Lu, X., Veefkind, P., de Laat, J., Kong, H., Wang, J., Sun, J., Ding, J., Zhao, Y., and Weng, H.: A New Divergence Method to Quantify Methane Emissions Using Observations of Sentinel-5P TROPOMI, *Geophys. Res. Lett.*, 48, e2021GL094151, <https://doi.org/10.1029/2021GL094151>, 2021.
- Lorente, A., Borsdorff, T., Butz, A., Hasekamp, O., aan de Brugh, J., Schneider, A., Wu, L., Hase, F., Kivi, R., Wunch, D., Pollard, D. F., Shiomi, K., Deutscher, N. M., Velazco, V. A., Roehl, C. M., Wennberg, P. O., Warneke, T., and Landgraf, J.: Methane retrieved from TROPOMI: improvement of the data product and validation of the first 2 years of measurements, *Atmos. Meas. Tech.*, 14, 665–684, <https://doi.org/10.5194/amt-14-665-2021>, 2021a.
- Lorente, A., Borsdorff, T., aan de Brugh, J., Landgraf, J., and Hasekamp, O.: SRON S5P – RemoTeC scientific TROPOMI XCH<sub>4</sub> dataset, Zenodo [data set], <https://doi.org/10.5281/zenodo.4447228>, 2021b.
- Luther, A., Kleinschek, R., Scheidweiler, L., Defratyka, S., Stanisavljevic, M., Forstmaier, A., Dandocsi, A., Wolff, S., Dubravica, D., Wildmann, N., Kostinek, J., Jöckel, P., Nickl, A.-L., Klausner, T., Hase, F., Frey, M., Chen, J., Dietrich, F., Necki, J., Swolkień, J., Fix, A., Roiger, A., and Butz, A.: Quantifying CH<sub>4</sub> emissions from hard coal mines using mobile sun-viewing Fourier transform spectrometry, *Atmos. Meas. Tech.*, 12, 5217–5230, <https://doi.org/10.5194/amt-12-5217-2019>, 2019.
- Luther, A., Kostinek, J., Kleinschek, R., Defratyka, S., Stanisavljević, M., Forstmaier, A., Dandocsi, A., Scheidweiler, L., Dubravica, D., Wildmann, N., Hase, F., Frey, M. M., Chen, J., Dietrich, F., Necki, J., Swolkień, J., Knote, C., Vardag, S. N., Roiger, A., and Butz, A.: Observational constraints on methane emissions from Polish coal mines using a ground-based remote sensing network, *Atmos. Chem. Phys.*, 22, 5859–5876, <https://doi.org/10.5194/acp-22-5859-2022>, 2022.
- Morcrette, J.-J., Boucher, O., Jones, L., Salmond, D., Bechtold, P., Beljaars, A., Benedetti, A., Bonet, A., Kaiser, J. W., Razinger, M., Schulz, M., Serrar, S., Simmons, A. J., Sofiev, M., Suttie, M., Tompkins, A. M., and Untch, A.: Aerosol analysis and forecast in the European Centre for Medium-Range Weather Forecasts Integrated Forecast System: Forward modeling, *J. Geophys. Res.-Atmos.*, 114, D06206, <https://doi.org/10.1029/2008JD011235>, 2009.
- Pandey, S., Houweling, S., Krol, M., Aben, I., Chevallier, F., Dlugokencky, E. J., Gatti, L. V., Gloor, E., Miller, J. B., Detmers, R., Machida, T., and Röckmann, T.: Inverse modeling of GOSAT-retrieved ratios of total column CH<sub>4</sub> and CO<sub>2</sub> for 2009 and 2010, *Atmos. Chem. Phys.*, 16, 5043–5062, <https://doi.org/10.5194/acp-16-5043-2016>, 2016.
- Pandey, S., Gautam, R., Houweling, S., van der Gon, H. D., Sadavarte, P., Borsdorff, T., Hasekamp, O., Landgraf, J., Tol, P., van Kempen, T., Hoogeveen, R., van Hees, R., Hamburg, S. P., Maasackers, J. D., and Aben, I.: Satellite observations reveal extreme methane leakage from a natural gas well blowout, *P. Natl. Acad. Sci. USA*, 116, 26376, <https://doi.org/10.1073/pnas.1908712116>, 2019.
- Climate Change 2014: IPCC: Synthesis Report. Contribution of Working Groups I, II and III to the Fifth Assessment Report of the Intergovernmental Panel on Climate Change, edited by: Core Writing Team, Pachauri, R. K., and Meyer, L. A., IPCC, Geneva, Switzerland, 151 pp., 2014.
- Saunois, M., Stavert, A. R., Poulter, B., Bousquet, P., Canadell, J. G., Jackson, R. B., Raymond, P. A., Dlugokencky, E. J., Houweling, S., Patra, P. K., Ciais, P., Arora, V. K., Bastviken, D., Bergamaschi, P., Blake, D. R., Brailsford, G., Bruhwiler, L., Carlson, K. M., Carrol, M., Castaldi, S., Chandra, N., Crevoisier, C., Crill, P. M., Covey, K., Curry, C. L., Etiope, G., Frankenberg, C., Gedney, N., Hegglin, M. I., Höglund-Isaksson, L., Hugelius, G., Ishizawa, M., Ito, A., Janssens-Maenhout, G., Jensen, K. M., Joos, F., Kleinen, T., Krummel, P. B., Langenfelds, R. L., Laruelle, G. G., Liu, L., Machida, T., Maksyutov, S., McDonald, K. C., McNorton, J., Miller, P. A., Melton, J. R., Morino, I., Müller, J., Murguía-Flores, F., Naik, V., Niwa, Y., Nöce, S., O'Doherty, S., Parker, R. J., Peng, C., Peng, S., Peters, G. P., Prigent, C., Prinn, R., Ramonet, M., Regnier, P., Riley, W. J., Rosentretter, J. A., Segers, A., Simpson, I. J., Shi, H., Smith, S. J., Steele, L. P., Thornton, B. F., Tian, H., Tohjima, Y., Tubiello, F. N., Tsuruta, A., Viovy, N., Voulgarakis, A., Weber, T. S., van Weele, M., van der Werf, G. R., Weiss, R. F., Worthy, D., Wunch, D., Yin, Y., Yoshida, Y., Zhang, W., Zhang, Z., Zhao, Y., Zheng, B., Zhu, Q., Zhu, Q., and Zhuang, Q.: The Global Methane Budget 2000–2017, *Earth Syst. Sci. Data*, 12, 1561–1623, <https://doi.org/10.5194/essd-12-1561-2020>, 2020.
- Schneider, M., Ertl, B., and Diekmann, C.: MUSICA IASI full retrieval product standard output (processing version 3.2.1), Institute of Meteorology and Climate Research, Atmospheric Trace Gases and Remote Sensing (IMK-ASF), Karlsruhe Institute of Technology (KIT) [data set], <https://doi.org/10.35097/408>, 2021.
- Schneider, M., Ertl, B., Tu, Q., Diekmann, C. J., Khosrawi, F., Röhling, A. N., Hase, F., Dubravica, D., García, O. E., Sepúlveda, E., Borsdorff, T., Landgraf, J., Lorente, A., Butz, A., Chen, H., Kivi, R., Laemmle, T., Ramonet, M., Crevoisier, C., Pernin, J., Steinbacher, M., Meinhardt, F., Strong, K., Wunch, D., Warneke, T., Roehl, C., Wennberg, P. O., Morino, I., Iraci, L. T., Shiomi, K.,

- Deutscher, N. M., Griffith, D. W. T., Velasco, V. A., and Pollard, D. F.: Synergetic use of IASI profile and TROPOMI total-column level 2 methane retrieval products, *Atmos. Meas. Tech.*, 15, 4339–4371, <https://doi.org/10.5194/amt-15-4339-2022>, 2022a.
- Schneider, M., Ertl, B., Diekmann, C. J., Khosrawi, F., Weber, A., Hase, F., Höpfner, M., García, O. E., Sepúlveda, E., and Kinnison, D.: Design and description of the MUSICA IASI full retrieval product, *Earth Syst. Sci. Data*, 14, 709–742, <https://doi.org/10.5194/essd-14-709-2022>, 2022b.
- Schepers, D., Guerlet, S., Butz, A., Landgraf, J., Frankenberg, C., Hasekamp, O., Blavier, J.-F., Deutscher, N. M., Griffith, D. W. T., Hase, F., Kyro, E., Morino, I., Sherlock, V., Sussmann, R., and Aben, I.: Methane retrievals from Greenhouse Gases Observing Satellite (GOSAT) shortwave infrared measurements: Performance comparison of proxy and physics retrieval algorithms, *J. Geophys. Res.-Atmos.*, 117, D10307, <https://doi.org/10.1029/2012JD017549>, 2012.
- Schneising, O., Buchwitz, M., Reuter, M., Vanselow, S., Bovensmann, H., and Burrows, J. P.: Remote sensing of methane leakage from natural gas and petroleum systems revisited, *Atmos. Chem. Phys.*, 20, 9169–9182, <https://doi.org/10.5194/acp-20-9169-2020>, 2020.
- Tu, Q., Hase, F., Schneider, M., García, O., Blumenstock, T., Borsdorff, T., Frey, M., Khosrawi, F., Lorente, A., Alberti, C., Bustos, J. J., Butz, A., Carreño, V., Cuevas, E., Curcoll, R., Diekmann, C. J., Dubravica, D., Ertl, B., Estruch, C., León-Luis, S. F., Marrero, C., Morgui, J.-A., Ramos, R., Scharun, C., Schneider, C., Sepúlveda, E., Toledano, C., and Torres, C.: Quantification of CH<sub>4</sub> emissions from waste disposal sites near the city of Madrid using ground- and space-based observations of COCON, TROPOMI and IASI, *Atmos. Chem. Phys.*, 22, 295–317, <https://doi.org/10.5194/acp-22-295-2022>, 2022.
- Varon, D. J., McKeever, J., Jervis, D., Maasackers, J. D., Pandey, S., Houweling, S., Aben, I., Scarpelli, T., and Jacob, D. J.: Satellite discovery of anomalously large methane point sources from oil/gas production, *Geophys. Res. Lett.*, 46, 13507–13516, <https://doi.org/10.1029/2019GL083798>, 2019.
- Veefkind, J. P., Aben, I., McMullan, K., Förster, H., de Vries, J., Otter, G., Claas, J., Eskes, H. J., de Haan, J. F., Kleipool, Q., van Weele, M., Hasekamp, O., Hoogeveen, R., Landgraf, J., Snel, R., Tol, P., Ingmann, P., Voors, R., Kruizinga, B., Vink, R., Visser, H., and Levelt, P. F.: TROPOMI on the ESA Sentinel-5 Precursor: A GMES mission for global observations of the atmospheric composition for climate, air quality and ozone layer applications, *Remote Sens. Environ.*, 120, 70–83, <https://doi.org/10.1016/j.rse.2011.09.027>, 2012.
- Wolff, S., Ehret, G., Kiemle, C., Amediek, A., Quatrevalet, M., Wirth, M., and Fix, A.: Determination of the emission rates of CO<sub>2</sub> point sources with airborne lidar, *Atmos. Meas. Tech.*, 14, 2717–2736, <https://doi.org/10.5194/amt-14-2717-2021>, 2021.
- World Meteorological Organisation, WMO greenhouse gas bulletin No. 16.23 Novembet 2020, <https://public.wmo.int/en/resources/library/wmo-greenhouse-gas-bulletin> (last access: 12 July 2022), 2020.